Time Tiling of Learned Stimulus-Based Decision Making in Dorsal CA1 in the Hippocampus

Ma, M.[1,8], Simoes de Souza, F.[1,2,8], Futia, G.L.[3], Anderson, S.R.[4], Riguero, J. [4,5], Tollin, D.[4,5], Gentile-Polese, A.[1], Platt, J.P.[6], Hiratani, N.[7], Gibson, E.[3,5] and Restrepo, D[1,5,*].

[1]Department of Cell and Developmental Biology, University of Colorado Anschutz Medical Campus, Aurora, CO, 80045, USA.
[2]Center for Mathematics, Computation and Cognition, Federal University of ABC, Sao Bernardo do Campo, SP, Brazil.
[3]Department of Bioengineering, University of Colorado Anschutz Medical Campus, Aurora, CO, 80045, USA.
[4]Department of Physiology and Biophysics, University of Colorado Anschutz Medical Campus, Aurora, CO, 80045, USA.
[5]Neuroscience Graduate Program, University of Colorado Anschutz Medical Campus, Aurora, CO 80045, USA.
[6]Department of Neurosurgery, University of Colorado Anschutz Medical Campus, Aurora, CO, 80045, USA.
[7]Department of Neuroscience, Washington University, St. Louis, MO 63110, USA

[8]These authors contributed equally to this work
*Correspondence: diego.restrepo@cuanschutz.edu

SUMMARY

Hippocampal neural activity encodes for external cues and their variable temporal relationships, which is thought to be necessary to construct maps of sequential experiences. Here we used multiphoton microscopy to image neural activity in pyramidal cells of dorsal CA1 (dCA1) in mice undergoing go-no go associative learning. We found that pyramidal cells responded differentially to the rewarded and unrewarded stimuli. Most pyramidal cells responded to the valence of the stimuli (is the stimulus rewarded?) and some cells responded to stimulus identity. The stimulus was decoded accurately from the activity of the neuronal ensemble within each session, and decoding accuracy increased substantially as the animal learned to differentiate the stimuli. Decoding the stimulus from individual pyramidal cell activity revealed time-tiling of the time for discrimination of the stimuli. This time-tiled representation of stimulus divergence in dCA1 by sequential neural dynamics likely constitutes a map used for decision-making in associative learning.

INTRODUCTION

The hippocampus provides real time encoding and retrieval of detailed context memories that enables reactions to a constantly changing environment (Wiltgen et al., 2010). This is accomplished by diverse and distributed neuronal activity encoding external features such as contextually referenced space and time and sensory stimuli, as well as features influenced by the animal's behavior such as speed and direction of motion (Buzsáki and Llinás, 2017; Buzsaki and Moser, 2013; Mau et al., 2018; Stefanini et al., 2020). This is a demanding task mediated by plastic circuits involved in associative learning (Gruart et al., 2015; Neves et al., 2008). For example, imagine you are cooking your favorite dish, paella, for a gathering with friends. You carefully set up your paella before your friends arrive relying on your sensory systems and memory, re-reading your recipe, sensing the aroma of the saffron, visually inspecting the arrangement of the dish and checking the temperature. Your friends arrive, and while the paella is cooking you need to rely on periodic reminders to check the dish, walk back to the kitchen where you evaluate the aroma, whether the rice is sticking to the paella pan, and assess when it is ready (a go-no go decision). This behavior takes place within a highly distracting context where you interact with your friends while making the decision whether the dish is ready.

Here we address the neural representation of associative learning in dorsal CA1 (dCA1), an area of the hippocampus involved in spatial learning and working memory tasks. The involvement of dCA1 in associative learning of stimulus discrimination in

head-fixed animals is still unclear (Biane et al., 2023; Li et al., 2017; Moser et al., 1993; Rangel et al., 2016; Strange et al., 2014; Taxidis et al., 2020). Responsiveness of dCA1 pyramidal cells to sensory stimuli have been reported to change with learning in animals undergoing an odorant discrimination associative learning go-no go task (Biane *et al.*, 2023; Li *et al.*, 2017). Li and co-workers showed that dCA1 pyramidal cells receiving connections conveying olfactory information from lateral entorhinal cortex (LEC) develop more selective spiking responses to odor cues during learning for mice engaged in an odor discrimination go-no go task and showed that optogenetic inactivation of the LEC to dCA1 connections slows learning in this task (Li *et al.*, 2017). In addition, Biane and colleagues find a learning-related increase in the proportion of cells responsive to rewarded (S+) odorant, but not to the unrewarded (S-) odorant, suggesting that stimulus representations in dCA1 are sensitive to perceived value. However, learning did not alter decoding accuracy that was already high before training in dCA1 (Biane *et al.*, 2023). Importantly, temporal patterning of dCA1 neural activity plays a key role in odorant working memory tasks (MacDonald et al., 2013; Taxidis *et al.*, 2020) and has been postulated to play a role in organizing memories (Eichenbaum, 2017) raising the question whether it contributes to the neural mechanism for go-no go associative learning in this brain region. Hippocampal “time cells” participate in conveying memory of the temporal order of events, working memory and signaling changes in temporal context (Eichenbaum, 2017; Shimbo et al.; Taxidis *et al.*, 2020). It has been hypothesized that the precise temporally structured activity of neurons make perceptually related responses coherent in time (Singer and Lazar, 2016), but it unknown whether there is time-tiled representation of *stimulus divergence* in dCA1 that

could contribute though sequential neural dynamics to behavioral responses reflecting decision-making in associative learning.

Here we use two-photon calcium imaging to evaluate ensemble decoding of stimuli from temporally patterned neural activity in dCA1 in mice engaged in an olfactory go-no go task where they receive a water reward after licking on a spout when presented with the S+ odorant and do not receive a water reward for the S- odorant (Ma et al., 2020) (Figure 1A). We characterized stimulus divergence of calcium responses of different cells (regions of interest, ROIs) from the calcium video by multivariate robust estimation (Hakan et al., 2021) and we assessed changes in neuronal activity after switching rewarded with unrewarded stimuli to determine whether the cells respond to the identity of the stimulus as opposed to its valence (is the stimulus rewarded?). Finally, we assessed the accuracy of decoding the stimuli with different subsets of cells and determined whether the onset of stimulus decoding reflecting divergence of stimulus responses was time-tiled.

RESULTS

Two-Photon Calcium Imaging in Dorsal CA1 in Head-Fixed Mice undergoing a Go-No Go Olfactory Associative Learning Task

Calcium imaging was performed through a GRIN lens in adult Thy1-GCaMP6f mice (n=4) expressing the calcium indicator GCaMP6f in pyramidal neurons in dCA1 (Figure

1A, Figure S1). Water-deprived mice started the trial by licking on the water spout. One of two odorants was delivered in random order 1-1.5 sec after the start of the trial and the odorant was presented for 4 sec. Mice were trained to respond to the rewarded odorant (S+) by licking at least once during two 2 sec response areas to obtain a water reward. The water reward was not delivered regardless of licking when the unrewarded odorant (S-) was presented. Two-photon calcium imaging movies were denoised (Li et al., 2023), motion-corrected (Pnevmatikakis and Giovannucci, 2017) and time-binned traces of nonnegative changes in fluorescence intensity ($\Delta F/F$) were obtained for multiple ROIs using EXTRACT, an algorithm based on robust estimation theory (Hakan *et al.*, 2021)(Figure 1B). Figures 1C,E show calcium imaging data from 153 ROIs recorded in dCA1 during a 20 min session for a mouse that was proficient in the go-no go task (proficient stage is defined as percent correct >= 80%). Figure S1A shows the differential lick response to S+ vs. S- in this session. As expected the fluorescence traces displayed calcium spikes whose timing was heterogeneous when evaluated by the cross correlation between the traces of all ROIs (Figure 1D). In this session a subset of the ROIs responded differentially during S+ vs. S- odorant trials (Figures 1C,E). Consistent with the heterogeneous response there was little difference between S+ and S- trials when the $\Delta F/F$ was averaged over all ROIs (Figure S1C). However, there was an increase in mean $\Delta F/F$ following trial start. These results suggest the existence of a complex time-structure underlying the calcium responses from a population of dCA1 neurons in the go-no go task.

135 **Mice Learn to Respond Differentially to the Rewarded and Unrewarded Odorants**
136 **in the Go-No Go Task**
137
138 In the first training session the percent correct response to the odorants was between
139 45% and 65% correct for three of four mice (Figure S2 A-C)(S+: 1% heptanal, HEP, S-:
140 mineral oil, MO) Percent correct was calculated as 100*(hits + CR)/number of trials, we
141 name the session as “learning stage” when percent correct behavior is between 45%
142 and 65% correct. We then trained the mice in 3-6 training sessions per day. As shown
143 in Figure S2 A-D the mice gradually reached the proficient stage (percent correct
144 behavior >80%). The fourth mouse became proficient in the first session (Figure S2D).
145 We recorded from a total of 18 learning stage sessions in three mice and a total of 66
146 proficient sessions in four mice. Once the mice had stable proficient performance the
147 odorants were reversed (S+: mineral oil, MO, S-: 1% HEP) to investigate whether dCA1
148 calcium responses are encoding the identity or valence of odorants. The percent correct
149 behavior dropped immediately below 50% and gradually recovered to proficient (>80%)
150 (Figure S2A-D). We recorded from a total of 25 forward proficient stage sessions and 41
151 reversed proficient stage sessions in four mice).
152
153 The go-no go task used in this study is an olfactory cued task where the animal starts a
154 trial by licking on the water spout. At the start of the trial a diverter valve turns on
155 directing the 2 lt/min air flow away from the nose cone towards an exhaust line (Figure
156 1A) and one of two odorant valves (S+ or S-) opens allowing the odorant, delivered at
157 50 ml/min, to equilibrate with the 2 lt/min background air flow. 1-1.5 sec after trial start

158 the diverter valve brings the air back to the nose cone resulting in a sharp increase in
159 odorant concentration providing the mouse with an odorant cue with an onset ~100
160 msec after reset of the diverter valve (Figure S3A). In the rest of the manuscript the time
161 when the diverter valve turns back to the odorant cone is time zero. Finally, turning on
162 the odorant valves at the start of the trial delivers a clicking sound that can be used to
163 decode the stimuli (see Methods and Figure S3 B-D). However, mice do not cue on the
164 click as shown by the fact that when the odorant is removed (but the odor valve still
165 clicks) the performance drops to 50% (Figure S2 E-G, consistent with previous studies
166 with the same olfactometer (Slotnick and Restrepo, 2005)).
167
168 Figure S4 illustrates lick behavior in learning and proficient stages for the four mice in
169 this study. Figures in S4A show the per trial time course for mean lick fraction for S+
170 and S- trials calculated for all sessions (18 learning stage and 66 proficient stage, 4
171 mice). The lick fraction is defined per time point as the fraction of trials within a session
172 when the lick is detected and ranges from zero (no licks detected) to one (a lick was
173 detected in every trial). Mice start the trial by licking on the water spout 1 to 1.5 sec
174 before odorant delivery evidenced by an increase in mean lick fraction before odorant
175 delivery (arrow in Figure S4A right panel). Mice in the learning stage start licking again
176 shortly before the odorant is delivered and the mean lick fraction starts diverging
177 between S+ and S- trials after about one second (Figure S4A, left panel). In order to
178 quantify when the lick behavior differs between S+ and S- we computed a p value of the
179 difference in S+ vs S- lick fraction using a ranksum test. The left panel in Figure S4B
180 shows that for mice in the learning stage the p value for lick divergence decreases

monotonically below 0.05 (black dashed line) when the water reward is delivered (first red vertical line). In contrast, for the proficient mice (Figure S4B, right panel) the mean lick fraction diverges between S+ and S- a fraction of a second after odorant delivery. Figure S4C shows the summary of mean lick fraction for different time windows within the trial. We find a sharp increase for proficient mice in the difference between S+ and S- trials in lick fraction during the odor period. We do not find a difference in lick fraction between S+ and S- trials during the pre time period (-1.5 to 0 sec) when the animal could use auditory cues. A generalized linear model (GLM) analysis yielded a statistically significant difference for the interaction between learning vs. proficient, time window and S+ vs S- for the odor and reinforcement windows (vs. baseline time window) ($p<0.001$) but there was no difference for this interaction for the pre time window ($p>0.05$), 744 observations, 725 d.f., 4 mice, GLM F-statistic=153, $p<0.001$ (Table S1). This lick behavior that becomes divergent between S+ and S- trials a fraction of a second after odorant delivery is consistent with a previous study performed with the same olfactometer (Ma *et al.*, 2020).

Taken together the data on 50% mouse performance in the absence of odorants (Figure S2E-G) and lick behavior (Figure S4) indicate that mice cue on odorants in this multisensory go-no go task.

n-Dimensional ΔF/F Space Expands before the Animal Starts the Trial and the Dimensionality of Neural Space Increases as the Animal Learns

The highly complex dynamics of dCA1 network provide a high-dimensional space for the accommodation of an immense repertoire of potential states. Presumably, the n-dimensional network dynamics collapses into stimulus specific metastable subregions detectable as manifolds that constrain the dynamic space in anticipation to the presentation of the stimulus reflected by anticipatory changes in dimensionality (Nieh et al., 2021; Singer and Lazar, 2016). We proceeded to evaluate changes in n-dimensional neural space where each dimension is the neural activity for each ROI quantified by z-scored $\Delta F/F$ calcium changes as a function of time within each trial ($z\Delta F/F$, Figure 2A). As a first step we evaluated overall changes in mean $z\Delta F/F$ averaged among all ROIs at each time step. Interestingly in this task where the mouse starts the trial by licking on the lick spout we found a substantial increase in the overall mean $\Delta F/F$ for both S+ and S- *before* the animal started the trial (pre window compared to baseline increased by ~50%, Figures 2B and C). There appeared to be a difference in the mean $z\Delta F/F$ between S+ and S- for proficient mice (Figure 2B). However, there was no statistical difference between S+ and S- trials in the mean $z\Delta F/F$ calculated in different time windows (Figure 2C). A GLM analysis yielded a statistically significant difference between the time windows (compared to baseline, $p<0.05$) but there was no difference between S+ and S- or between learning and proficient stages ($p>0.05$), 744 observations, 725 d.f., 4 mice, F-statistic=34.6, $p<0.001$ (Table S2).

We then assessed whether there were changes in the overall volume of n-dimensional space where each dimension is defined as the axis depicting $z\Delta F/F$ for each ROI at each time point evaluated for each trial (Figure 2A). To assess changes in n-

227 dimensional volume we calculated at each time point the Euclidean distance (Edelman,
228 1998) between z∆F/F for each S+ and all other S- trials (we name this distance
229 “between S+ and S-“) as opposed to the Euclidean distance between z∆F/F for each
230 pair of S+ trials or between z∆F/F for each pair of S- trials (“within S+ or S-“). The
231 increase in mean z∆F/F shown in Figure 2B and C was mirrored by an increase in the
232 mean Euclidean distance calculated either “between S+ and S-“ or “within S+ or S-“
233 (Figure 2D). This increase in Euclidean distance had an onset slightly before trial start
234 indicating that there was an expansion of n-dimensional neural space as the animal
235 prepared to start the trial. This increase started decreasing when the odorant was
236 presented and subsided by the end of the trial ~15 seconds after trial start. A GLM
237 analysis of the Euclidean distance calculated for the different time windows (Figure 2E)
238 yielded a statistically significant difference for Euclidean distance calculated in the
239 different time windows (compared to baseline, $p<0.05$), but there was no difference
240 comparing “between S+ and S-“ vs “within S+ or S-“ or between learning and proficient
241 stages ($p>0.05$), 744 observations, 725 d.f., 4 mice, GLM F-statistic=36.6, $p<0.001$
242 (Table S2).
243
244 Finally, in order to understand changes in overall n-dimensional space information
245 content we estimated the dimensionality of the n-dimensional neural space (Litwin-
246 Kumar et al., 2017). Dimensionality is a convenient measure to quantify representation
247 of information in a neural layer (in this case CA1) that received mixed sensory and
248 motor inputs. Its value ranges from the number of ROIs if all display independent
249 uncorrelated activity to one if all ROIs display correlated activity. Dimensionality is

closely related to classification performance of a decoder. Figures 2F-G show that the dimensionality is constant within trials and that learning elicits an increase in dimensionality. A GLM analysis of the per time window dimensionality data shown in Figure 2G yielded a statistically significant difference for dimensionality for learning stage vs. proficient stage ($p<0.05$), but there was no difference comparing the pre (-1 to 0 sec) and odor (3.1 to 4.1 sec) time windows ($p>0.05$), 184 observations, 177 d.f., 4 mice, GLM F-statistic=15.4, $p<0.001$ (Table S3). These results indicate that dimensionality of the initially unconstrained n-dimensional neural space increases as the mouse's dCA1 network changes with learning.

Demixed Principal Component Analysis (dPCA) Reveals Increased Differential Response to Stimuli upon Learning

Mean z∆F/F did not differ between S+ and S- trials, and did not change with learning (Figures 2B-C). This is not surprising given the heterogeneity of CA1 neural activity (e.g. Figure 1D). In order to perform an assessment of changes in neural activity with learning and differences in activity between rewarded (S+) and unrewarded (S-) stimulus trials we proceeded to assess changes in neural activity after dimensionality reduction. We performed a demixed principal component analysis (dPCA) (Kobak et al., 2016) of the z∆F/F population data per mouse to evaluate changes in principal components quantifying neural activity in the axis maximizing stimulus variance. An example of dPCA for a proficient mouse is shown in Figure S5. dPCA estimates stimulus components (Figure S5E) and stimulus-independent components (Figure S5F).

Figure S5A and B show the explained variance of the first 10 components. We used the sum of stimulus components to estimate the divergence of S+ vs. S- trial component and their changes with learning. Figure S5Di shows that the sum of stimulus components diverged shortly after trial start. As expected, the sum of independent components did not differ between S+ and S- trials (Figure S5Dii).

Figure 3 shows the results of dPCA analysis for all mice. The sum of the stimulus principal components diverged between S+ and S- trials shortly after trial start and the magnitude of the divergence increased as the animal learned (Figure 3A and B). The sum of stimulus-independent components did not differ between stimuli and did not display changes as a function of time (Figure 3C and D). A GLM analysis yielded for the sum of the stimulus principal components a statistically significant difference for the interaction between the learning vs. proficient stages and the odor time window (or the reinforcement time window) vs. the baseline time window and for the interaction between S+ and S-, the odor time window (or reinforcement window) vs. the baseline time window and the learning vs. proficient stages ($p<0.01$), 48 observations, 32 d.f., 4 mice, GLM F-statistic=10.6, $p<0.001$ (Table S4). The GLM analysis did not yield statistically significant changes between S+ and S- or for the odor time window for stimulus-independent components (Table S4).

Stimulus-divergent zΔF/F Responses are Heterogeneous, Divergence Increases with Learning and the Onset of Divergence Takes Place at Discrete Times

296 The results of dPCA shown in Figure 3 indicate that there is a substantial increase in
297 the divergence between S+ and S- as the animal learns. We proceeded to ask whether
298 this divergence of the responses is heterogeneous when assessed on a per ROI basis.
299 We classified z∆F/F responses in S+ or S- trials within a session when the difference in
300 z∆F/F between a baseline time window (-3 to -1.5 sec) and a response window (-1 to
301 5.5 sec) was found to be significantly different when tested with a GLM with time and
302 time window as the two independent variables. The GLM was calculated for each ROI
303 within all sessions belonging to the learning or proficient stages for the four mice in this
304 study and the p value for significance was corrected for multiple comparisons using a
305 false discovery rate (Curran-Everett, 2000). Figure 4A shows the time courses for z∆F/F
306 for S+ and S- trials for all divergent ROIs for the proficient stage and Figure 4C shows
307 the cross correlogram of the z∆F/F time courses. We sorted the time courses into three
308 clusters using a hierarchical binary cluster tree. The average z∆F/F time courses for the
309 three clusters are shown in Figure 4E. Cluster 1 displayed a bimodal time course where
310 z∆F/F for S+ increased above S- shortly after trial start and this reversed after the
311 reward when S- increased above S+. Cluster 2 displayed an increase in z∆F/F for S+
312 and a decrease for z∆F/F for S- shortly after trial start. Cluster 3, that was the cluster
313 with the largest number of ROIs displayed a robust increase in z∆F/F for S- and a
314 smaller increase for S+. Therefore, time courses for z∆F/F for divergent ROIs for the
315 proficient stage display substantial heterogeneity.
316
317 Analysis of z∆F/F divergent ROIs for the learning stage also displayed a similar
318 heterogeneity in time courses (Figure S6B). The percent of divergent ROIs had a

319 tendency to be smaller for the learning stage, but was not significantly different
320 compared to the proficient stage (Figure 4D, t-test, $p>0.05$, 3 mice for learning, 4 mice
321 for proficient). However, when the z∆F/F was tested with GLM analysis for statistically
322 significant differences using learning stage and S+ vs. S- as independent variables
323 (Figure S6D) there were statistically significant differences for learning stage and the
324 interaction of learning stage and S+ vs. S- for the peak of S- for cluster 1, for the
325 interaction of learning stage and S+ vs. S- for cluster 2 and for learning stage and the
326 interaction of learning stage and S+ vs. S- for cluster 3 ($p<0.05$, number of
327 observations, d.f. and F statistics are in Table S5). This indicates that there are changes
328 in z∆F/F time course elicited by learning.
329
330 Finally, responses of a subset of CA1 pyramidal cells that have been named odor-
331 specific time cells take place at discrete time points in the delay period in a delayed
332 non-match to sample task where the animal receives a reward when they respond in
333 trial where the second odor differs from the first odor (Taxidis *et al.*, 2020)(also see
334 (MacDonald *et al.*, 2013). Interestingly, perusal of the pseudocolor time courses for
335 z∆F/F in Figure 4A appeared to show differences in time onset of the divergence. We
336 assessed the divergence time for each divergent ROI. Figure S6A shows examples of
337 the time course for z∆F/F for a subset of ROIs. The divergence takes place at discrete
338 time points after the start of the trial ranging from onset of divergence close to the start
339 of the trial (Figure S6A ii) to onset close to the time when the reward was delivered
340 (Figure S6C vi). Figure 4B shows histograms of the divergence times for the learning
341 and proficient stages. The divergence times spanned the time period from trial onset to

342 times after the reward is delivered. The divergence times for the learning stage took
343 place at earlier times than those for the proficient stage (ranksum $p<0.001$, 99
344 divergence time bins in the histograms).
345
346 **Switching the Rewarded Stimulus to Unrewarded Elicits Changes in z∆F/F**
347 **Stimulus Responses Consistent with Response to the Valence of the Stimulus**
348
349 In order to determine whether stimulus-divergent z∆F/F responses are divergent
350 responses to the stimulus identity (odorant identity or odorant valve click) vs. stimulus
351 valence (are the stimuli rewarded?) we switched the rewarded S+ stimulus (1%
352 heptanal, HEP) with the unrewarded S- stimulus (mineral oil, MO) after the animal
353 became proficient. We call this a switch from a forward go-no go task when HEP was
354 S+ to a reversed go-no go task where MO became S+. As shown in Figures S2A-D
355 after this stimulus reversal the percent correct behavior decreased below 50%, and
356 subsequently recovered eventually reaching >80% indicating that the animal learned the
357 new reversed valence of the stimulus. Figure 5A shows the z∆F/F time course for ROIs
358 that responded with divergence to the stimuli when the animal was proficient in the
359 forward task. As performed for z∆F/F time courses in Figure 4 we performed a cross
360 correlation analysis for this forward task (shown in Figure S7C) and we sorted the time
361 courses into three clusters using a hierarchical binary cluster tree. The average z∆F/F
362 time courses for cluster 2 that responded with a large increase to S- is shown in Figure
363 5C and the average time courses for the other clusters are shown in Figure S7A and B.
364 As in Figure 4 the responses to S- (MO) tended to be larger than responses to S+

365 (HEP) in the most abundant cluster of responses (cluster 3) in this forward task (Figure
366 5A).
367
368 Interestingly, Figures 5A-D show that when we reversed the stimuli the majority of the
369 divergent z∆F/F time courses still responded with larger increases for the S- stimulus
370 (cluster 2, now switched to HEP, also see mean z∆F/F time courses for each cluster in
371 Figures 5D and S7A,B). Therefore in both the forward and reversed tasks the
372 unrewarded odorant stimuli elicited a larger z∆F/F response in a large portion of cluster
373 2 ROIs when the animal was proficient. We quantified this shift in z∆F/F time courses
374 with reversal by determining the peak value for stimulus-induced changes in z∆F/F.
375 Figure 5D shows a bar graph of the peak changes in z∆F/F for forward and reversed
376 runs for cluster 2 and Figure S7Aiii and Biii shows the results for clusters 1 and 3. When
377 the z∆F/F peak values were tested with GLM analysis for statistically significant
378 differences using odorant and forward vs. reversed as independent variables there were
379 statistically significant differences for both odorant and forward vs. reversed ($p<0.001$,
380 number of observations, d.f. and F statistics are in Table S6). These data suggest that
381 the majority of the z∆F/F stimulus responses are responses to the odorant value (is the
382 odorant rewarded?) as opposed to the odorant identity.
383
384 We proceeded to determine for the mouse whose percent correct behavior is shown in
385 Figure S2D the z∆F/F divergent responses for ROIs whose location was matched
386 across the last proficient forward vs. the first reversed proficient session. We were able
387 to match the ROIs because all of these sessions were recorded the same day. Figure

388 S8A shows divergent z∆F/F responses for matched ROIs in forward and reversed
389 reward proficient sessions and Figure S8C shows the d' time course calculated for HEP
390 vs. MO for these divergent z∆F/F responses. d' was calculated on a per time point basis
391 for z∆F/F time courses for HEP vs. MO. As defined (see methods), a change in d'
392 polarity indicates that the response is a response to the valence. Figure 5E shows a plot
393 of the peak value of d' in the odorant period for the forward and reversed runs for all the
394 matched ROI divergent z∆F/F responses shown in Figure S8C. Most of the d' values
395 reverse polarity with the forward to reversed switch indicating that these ROIs represent
396 the odorant value. However, a smaller number kept polarity of the response as the
397 odorant reward was reversed indicating that a smaller number of ROIs does respond to
398 the stimulus identity. In conclusion, for proficient sessions (>80% correct behavior) most
399 of the z∆F/F divergent ROIs represent stimulus valence, and a smaller number of ROIs
400 respond to the odorant identity.
401
402 **The Accuracy for Decoding the Stimulus Increases with Learning and is**
403 **Dependent on the Fit Window**
404
405 We asked whether the information embedded within z∆F/F activity of all ROIs can be
406 used to decode the stimulus (S+ vs. S-). Figure 6 shows the time courses for GLM
407 decoding of stimulus identity (other decoding algorithms yielded similar results, see
408 Figure S9). GLM was trained with different time windows using z∆F/F activity of all ROIs
409 in all S+ and S- trials within each session to evaluate the dependence of decoding
410 accuracy per trial on the information embedded within particular time windows. As a

411 control time courses for accuracy are shown where the trial identity (S+ or S-) was
412 shuffled (red time courses in i and ii panels and light grey bars in iii panels in Figure 6).
413 When we trained the GLM using a broad fit time window spanning the odorant period
414 and the beginning of the reward period (0.5 to 5.5 sec) decoding accuracy started
415 increasing above 0.5 slightly after trial start (~-1 sec) and reached ~0.8 through a
416 window spanning the later 3 sec of the odorant window for the proficient animal (Figure
417 6Aii). In contrast, the decoding accuracy for the learning stage only reached ~0.65
418 (Figure 6Ai). The bar graph in Figure 6Aiii shows the data for pre (-1 to 0), odor (3.1 to
419 4.1) and reinforcement (4.5 to 5.5) time windows. A GLM analysis yielded a statistically
420 significant difference for odor and reinforcement time windows vs. pre window and for
421 the interaction between these time window comparisons and proficient vs. learning
422 stages ($p<0.05$-0.001), 279 observations, 270 d.f., 4 mice, GLM F-statistic=37.7,
423 $p<0.001$ (Table S7).
424
425 We then asked how the decoding accuracy time course varies depending on the fit time
426 window. As expected when we the fit window spanned a time period before stimulus
427 presentation (-5 to -3 sec) accuracy did not increase above shuffled (Figure 6C, the p
428 value for GLM was >0.5 for all comparisons, see Table S7). In contrast, when the
429 window spanned the reinforcement period (4.5 to 6.5 sec) decoding increased above
430 0.5 for the learning stage after the mouse was given the reinforcement (Figure 6Bi) and
431 the increase in decoding accuracy above 0.5 shifted to the time when the odorant was
432 presented when the mouse became proficient (Figure 6Bii). GLM analysis of the bar
433 graph in Figure 6Biii yielded a statistically significant difference for odor and

434 reinforcement time windows vs. pre window and for the interaction between odor
435 window vs. pre window and proficient vs. learning stages ($p<0.05$-0.001), but was not
436 significant for the interaction between reinforcement window vs. pre window and
437 proficient vs. learning stages 279 observations, 264 d.f., 4 mice, GLM F-statistic=45,
438 $p<0.001$ (Table S7). Finally, when the fit window was a narrow window at the end of the
439 odorant period (2 to 4 sec) the increase in accuracy for the proficient mice did not reach
440 a plateau during the odorant window (Figure 6D, see GLM results in Table S7). The
441 results indicate that $z\Delta F/F$ activity of all ROIs contains information sufficient to decode
442 the stimuli and that, as expected this information differs when different time windows are
443 used to fit the GLM decoding algorithm.
444
445 **Between Trials Stimulus Decoding is Biased to Predict the Unrewarded Stimulus**
446 **and there are Sudden Brief Replays of Rewarded Stimulus Prediction**
447
448 Hippocampal offline replay of neural patterns plays a role in spatial learning (Michon et
449 al., 2019; Singer et al., 2013). We explored whether replay of neural activity for stimulus
450 decoding happened between trials for proficient mice engaged in the go-no go task.
451 Figure 7A shows a time course for prediction of the stimuli by GLM decoding calculated
452 during an imaging session. As in Figure 6A, GLM was fit to neural activity for all ROIs
453 during the 0.5 to 5.5 sec spanning most of the odorant window. A prediction value of 1
454 corresponds to S+ prediction and a value of 0 represents S-. The blue shade shows the
455 5th to 95th percentile band for prediction calculated after shuffling the stimulus labels. As
456 expected prediction increases to 1 for a period of time longer than the odorant window

during S+ trials while it increases briefly at the start of S- trials but returns to zero before the end of the odorant period. Figure 7B shows the mean prediction time course for all trials in proficient sessions for the 4 mice (a total of 1848 trials). For this within trial decoding the prediction starts increasing before trial start for both the S+ and S- trials and it diverges between S+ and S- at the start of the trial. The bar graph in Figure 7C shows the prediction for S+ and S- in a baseline period (-2.5 to -1.5) and an odor period (2 to 4.1 sec). A GLM analysis yields significant differences for baseline vs. odor time windows and for the interaction between S+ vs. S- and time windows, $p<0.001$, 4 mice, 220 observations, 213 d.f., F-statistic 194, $p <0.001$ (Table S8).

Interestingly, the average prediction is lower than shuffled in between trials (Figure 7A and 7D) indicating that the default decoding is S- for most of the time between trials (GLM p value for between vs. shuffled <0.001, 110 observations, 105 d.f., F-statistic 70.7, $p<0.001$, Table S8). However, there are clear brief shifts of prediction to 1 (predicting S+, e.g. arrow in Figure 7A). We identified these spontaneous shifts of prediction from 0 to 1 in between trials by finding increases beyond the 95 percentile of the shuffled prediction values (blue shade in Figure 7A). We found a total number of 1635 spontaneous shifts to S+ prediction. The duration of these spontaneous shifts in prediction varied between a fraction of a second to two seconds (example in Figure 7A). The blue bounded line in Figure 7E shows the mean time course for the between trial spontaneous shifts in prediction compared to an adjacent time period with no spontaneous changes in prediction (“no change”, magenta). The bar graph in Figure 7F shows a large difference between the prediction before the onset of the spontaneous

increase in prediction to the peak of prediction for the spontaneous shift. A GLM analysis yields significant differences for spontaneous vs. no change and for the interaction between spontaneous vs. no change and baseline vs. peak time windows, $p<0.001$, 4 mice, 192 observations, 185 d.f., F-statistic 703, $p<0.001$ (Table S8).

Finally, we calculated the correlation between z∆F/F time courses for spontaneous shift and z∆F/F time courses for either S+ or S- trials for all ROIs within each session to determine whether the neural activity underlying the spontaneous prediction shifts from S- to S+ are more correlated with S+ vs S-. Figure 7G shows the time courses for the average correlations. The correlation of spontaneous z∆F/F with S+ diverges from the correlation with S- shortly after the start of the trial and remains high for a few seconds after reward. A GLM analysis yields significant differences in average correlations for comparison of the time windows (baseline vs. odor) and for the interaction between S+ vs. S- and time window, $p<0.001$, 4 mice, 216 observations, 209 d.f., F-statistic 15.7, p value <0.001 (Table S8). The sudden shift in prediction from S- to S+ in between trials and the fact that z∆F/F activity during these spontaneous shifts corelates with z∆F/F neural activity for S+ suggest that these events are replay of neural activity for the rewarded stimulus.

Decoding of Decision Making in the Go-No Go Task from CA1 Neural Activity is Time Tiled

502 Divergence of z∆F/F responses between S+ and S- stimuli takes place at different times
503 after trial start (Figure 4C) suggesting that stimulus decoding from neural activity is time
504 tiled. In order to assess time tiling of the time for decision making (is the stimulus S+ or
505 S-), we performed an analysis of the time course of stimulus decoding from z∆F/F
506 responses of *subsets of ROIs* per session for mice proficient in the go-no go task. The
507 number of ROIs used to calculate GLM decoding per session was varied from 1, 2, 5 to
508 15 ROIs per session and the results were compared to decoding with all ROIs in each
509 session. We first performed a visual survey of the within trial dynamics of stimulus
510 decoding accuracy when the decoding was performed with z∆F/F responses of single
511 ROIs (Figure S10). We found that decoding accuracy for different ROIs increased at
512 different times after trial start and reached accuracy values above 0.65. Three examples
513 of decoding accuracy time courses and their corresponding z∆F/F time courses for S+
514 and S- trials are shown Figure S10 A-C. In Figure S10 A accuracy increases to ~0.6 at
515 the start of the trial (immediately following valve click and before odorant addition) and
516 increases to a higher value (~0.8) after odorant presentation. In Figures S10 B and C
517 there is no increase in accuracy at the start of the trial and accuracy increases either
518 shortly after odorant addition (Figure S10 B) or ~3 sec after odorant addition (Figure
519 S10 C). A histogram of average accuracy values computed during the odor window (3.1
520 to 4.1 sec) showed a clear difference between S+ and S- trial z∆F/F for these three
521 examples (Figures S10 A-Ciii). In addition, we found a subset of ROIs whose decoding
522 yielded decreases in accuracy below 0.5. An example is shown in Figure S10 D where
523 the accuracy decreased to ~0.1. These decreases in accuracy took place for ROIs with
524 largely overlapping S+ and S- odorant period z∆F/F values with the exception of one or

525 two trials where the z∆F/F deviated from the other trials as evidenced in the histogram
526 in Figure S10 Diii.
527
528 We then performed stimulus decoding analysis with subsets of ROIs for the entire
529 dataset for mice proficient in the go-no go task (four mice, 66 sessions). Figure 8A
530 shows histograms of decoding accuracy calculated in the odor window (3.1 to 4.1 sec)
531 for stimulus decoding performed with z∆F/F from subsets of ROIs. As the number of
532 ROIs per decoding run is decreased stimulus decoding accuracy decreases (compare
533 Figure 8Av with 8Ai). In addition, accuracies calculated in the pre window (-1 sec to 0
534 sec) are smaller than accuracies calculated in the odor window (compare Figures 8A
535 and 8B) and the pre accuracies also appear to decrease as the number of ROIs per
536 decoding run is decreased (compare Figure 8Bv with 8Bi). A GLM analysis yields
537 significant differences in decoding accuracy for comparisons between the number of
538 ROIs and the time windows, $p<0.001$, 4 mice, 27344 observations, 27344 d.f., F-statistic
539 798, p value <0.001 (Table S9).
540
541 In the histograms shown in Figures 8A and B a subset of the accuracy values fall below
542 0.5 for decoding runs with smaller numbers of ROIs (see for example Figure 8 Ai). As
543 explained above and shown in Figure S10 Diii for these accuracy decreases the z∆F/F
544 odorant period values overlap for many of the S+ and S- trials, while they diverge for
545 one or two trials. However, for the odorant window a large number of decoding accuracy
546 values remain above 0.65 for decoding with small ROI numbers. For example for
547 decoding with a single ROI 5.8% out of 6713 ROIs yield odor window accuracy above

548 0.65 (Figure 8 Ai). We proceeded to quantify the divergence time for each decoding
549 accuracy time course with odor window decoding accuracy >0.65. Divergence time was
550 calculated as the time after trial start when accuracy increased above 0.55 for at least
551 0.2 sec. Figure S11 shows for one session the divergence times estimated using this
552 method for all decoding accuracy time courses calculated with z∆F/F from single ROIs
553 that yield odor accuracy above 0.65. Histograms of these divergence times are shown
554 in Figure 8C for the different multiple ROI decoding sessions. The divergence times
555 decrease as the number of ROIs used for decoding calculation is increased (Figure 8C).
556 A GLM analysis of divergence times yields significant differences for comparisons
557 between accuracies calculated with different numbers of ROIs, $p<0.001$, 4 mice, 27354
558 observations, 27349 d.f., F-statistic 1400, p value <0.001 (Table S9). Finally, Figure 8D
559 shows all the decoding accuracy time courses with odorant decoding accuracy >0.65
560 calculated with a single ROI (Figure 8 Di) or all ROIs (Figure 8 Diii) sorted by
561 divergence time. For the single ROI decoding there is a large shift in the start of the
562 increase in accuracy (Figure 8 Di). Computing average accuracy time courses for
563 different divergence time windows shows that the onset of the increase in decoding
564 accuracy is time tiled and that decoding accuracy calculated for the earliest divergence
565 time window is biphasic with a small increase at trial start followed by a larger increase
566 after odor onset (Figure 8 Dii). These data show that the onset of increases in decoding
567 accuracy, quantifying time of decision making, is time tiled in hippocampal CA1
568 suggesting that these are decision making time cells.
569

570 **Lick Decoding and Stimulus Decoding Differ in their Relationship to Lick**
571 **Behavior**
572
573 Next we asked how stimulus decoding prediction is related to lick behavior (quantified
574 as lick fraction defined per time point as the fraction of trials when the animal was
575 making contact with the lick tube). We expected to find differences between stimulus
576 decoding and lick fraction because the accuracy of stimulus decoding starts increasing
577 above shuffled at trial start, before odorant is presented (Fig. 6A) and, in contrast,
578 licking starts diverging between S+ and S- after the odorant is delivered (Figs. S4A and
579 9A). In addition, we asked whether it was possible to decode lick behavior from neural
580 activity and whether the relationship between lick prediction and lick fraction differed
581 from the relationship between stimulus prediction and lick fraction. We performed this
582 analysis separately for different trial types classified on behavioral outcome: correct
583 responses (hits and correct rejections, CRs) and incorrect responses (miss and false
584 alarms, FAs)(Figure 1A).
585
586 Figure 9A shows the time course for lick fraction for the four types of trials. For all trial
587 types there was a transient increase in lick fraction when the animal started the trial by
588 licking on the water spout (arrow in Figure 9A). For hits (red) this transient increase was
589 followed by a steady increase in lick fraction during the odor period (0-4 sec) while for
590 CR trials (blue) there was a decrease toward zero shortly after odorant presentation. In
591 contrast, for miss trials lick fraction did not increase during the first second of the
592 odorant period (cyan), and for FA trials lick fraction was high for the first half of the

odorant period (magenta). Figure 9B is a bar graph showing the mean lick fraction during the first and second 2 sec response areas (RAs) during the odorant period (RAs are defined in Figure 1A). A GLM analysis yields significant differences in mean lick fraction for comparisons between CR or miss vs. FA or hit and for the interaction of miss or hit and FA and the RAs, $p<0.001$, 4 mice, 452 observations, 441 d.f., F-statistic 36.7, p value <0.001 (Table S10).

The accuracy for decoding lick fraction from $z\Delta F/F$ for all ROIs per session when the mice were proficient (four mice, 66 sessions) is shown in Figure S12. In contrast with accuracy for stimulus decoding that starts diverging from shuffled at the trial start before the odorant is presented (Fig. 6A) lick decoding accuracy starts diverging from shuffled after odorant presentation (Fig. S12A). The bar graph in Figure S12B shows the mean lick decoding accuracy data for pre (-1 to 0), odor (3.1 to 4.1) and reinforcement (4.5 to 5.5) time windows. A GLM analysis yielded a statistically significant difference for odor and reinforcement time windows vs. pre window and for the interaction between these time window comparisons and shuffling ($p<0.001$), 378 observations, 369 d.f., 4 mice, GLM F-statistic=62.1, $p<0.001$ (Table S10). Figures 9C and D show the lick prediction time course and mean lick prediction calculated in the RA windows for the different trial types (hit, miss, CR and FA). A GLM analysis yields significant differences in mean lick prediction for comparisons between hit or miss and FA and for the interaction of hit and FA and the RAs, $p<0.001$, 4 mice, 488 observations, 477 d.f., F-statistic 24.3, p value <0.001 (Table S10).

616 Figure 9E shows the time course for stimulus prediction for the four types of trials. For
617 hits (red) there was a steady increase in stimulus prediction that started at trial onset
618 and leveled to a value of ~0.8 during the odor period for hits (red) while for CR trials
619 (blue) there was an initial increase after trial start that decreased to ~0.2 during the odor
620 period. For miss trials stimulus prediction appeared to increase to a value below hit
621 prediction (cyan), and for FA trials stimulus prediction started increasing at trial start, but
622 did not decrease to ~0.3 during the odor period (magenta). Figure 9D is a bar graph
623 showing the mean stimulus prediction during the first and second 2 sec response areas
624 (RAs) during the odorant period. A GLM analysis yields significant differences in mean
625 stimulus prediction for comparisons between CR, miss or hit and FA, $p<0.05$, 4 mice,
626 452 observations, 441 d.f., F-statistic 57.3, p value <0.001 (Table S10).
627
628 The time course for lick fraction (Figure 9A) appears to be similar to the time course for
629 lick prediction (Figure 9C) and appears to differ from stimulus prediction (Figure 9E). In
630 order to get information on whether there is a common monotonic relationship between
631 lick fraction and stimulus prediction we plotted the mean lick fraction and mean stimulus
632 prediction calculated during each second of the odor period. The relationship between
633 lick fraction and lick prediction was linear (Figure 9G). In contrast, the relationship
634 between lick fraction and stimulus prediction differed between hit/miss and CR/FA
635 (Figure 9H). For hits and miss the stimulus/lick fraction relationship was linear (Figure
636 9E, cyan and red circles) while CR/FA points (Figure 9E, magenta and blue circles) the
637 relationship appeared to be quadratic and the points did not fall along the hit/miss line.
638 Therefore, the relationship between lick fraction and stimulus prediction in CA1 does not

follow the simple linear relationship that is expected from neural activity closely related to motor action. Rather, the relationship differs strikingly for S+ vs. S- stimuli. However, decoding lick behavior from the same neural activity did yield a prediction that showed a linear relationship with lick fraction.

DISCUSSION

In this study head-fixed mice engage in an associative learning go-no go task where they decide whether they lick to obtain a reward when presented with rewarded (S+) or unrewarded (S-) odorants at concentrations below irritant (trigeminal) threshold (Schaper, 1993). Unlike other sensory systems, the efferent axons from the olfactory bulb bypass the thalamus and synapse (directly or through relay in piriform cortex) onto the LEC that constitutes a major sensory input to dCA1 (Imai, 2014; Witter et al., 2017). Indeed, before it was realized that the hippocampus plays a key role in learning, Ramón y Cajal called the hippocampal formation the “quaternary” olfactory system because of this lack of relay through thalamus (Cajal, 1901). Olfactory responses mediated by LEC input are particularly prominent in the mouse dCA1 (Igarashi et al., 2014; Manns et al., 2007; Wood et al., 1999) and odorant responses in dCA1 are known to be involved in tasks such as delayed match/non match to sample (working memory)(MacDonald *et al.*, 2013; Taxidis *et al.*, 2020), odor place associative learning (Igarashi *et al.*, 2014), odorant gradient navigation (Radvansky and Dombeck, 2018) and odorant sequence evaluation (Martinez et al., 2019).

662 Dorsal CA1 is arguably one of the most studied areas of the brain involved in learning
663 and memory (Basu and Siegelbaum, 2015; Citri and Malenka, 2008; Fanselow and
664 Dong, 2010) and it is well documented to play a role in spatial and episodic learning and
665 memory (Eichenbaum, 2017; Moser *et al.*, 1993). Yet, its role in go-no go associative
666 learning has been called into question. Li et al. found that calbindin positive pyramidal
667 neurons in CA1 became more selective for odorants as animals became proficient in
668 the go-no go task and optogenetic inhibition of these cells slowed learning (Li *et al.*,
669 2017). In contrast, a study by Biane and co-workers found that the accuracy of odor
670 decoding in dCA1 was not altered by learning in the go-no go task (Biane *et al.*, 2023).
671 Here we find that there is a substantial increase in stimulus decoding accuracy when
672 the animal becomes proficient in the go-no go task (Figure 6); that learning results in
673 increased stimulus divergence of zΔF/F responses for single cells (Figure 4) and that
674 learning elicits an increase in the stimulus divergence of stimulus components in
675 demixed PCA (Figure 3). Our results are consistent with a role for dCA1 pyramidal cells
676 in go-no go associative learning proposed by Li et al. and with local field potential
677 recordings in dCA1 that find increased beta power (Martin et al., 2007) and increased
678 theta-referenced beta and gamma power (Ramirez-Gordillo et al., 2022) upon learning
679 in dCA1 in the go-no go associative learning task.
680
681 The go-no go task in this study also presents the animal with an auditory cue delivered
682 by opening one of two odorant valves at the start of the trial, 1 to 1.5 sec before the
683 odorant is delivered (Figures 1A and S3). Using dCA1 neural activity we were able to
684 decode, albeit with low accuracy, this differential stimulus at the start of the trial (arrow

in Figure 8Dii, Figure S10Ai). The hippocampus is known to respond to auditory cues (Aronov et al., 2017). Interestingly, even though we find that the information on the odor valve click is represented by neural activity in dCA1, when we removed the odorants the behavioral performance of the mice dropped to 50% (Figure S2E-G). Therefore, although this auditory information is present in CA1 it is not used by these animals as a stimulus cue in the go-no go task. In addition, for proficient mice lick fraction prediction in error trials in lick decoding differs from prediction for stimulus decoding (compare Figures 9D and F, and Figures 9G and H). Indeed, prediction for stimulus decoding tends to represent the correct stimulus even when the animal makes a mistake (Figure 9F) whereas for lick decoding the predictions for errors align closer with the mistakes the animal makes in the lick response (compare Figure 9D with Figure 9B). Likely the animal does perceive the odorant, but is satiated and makes a mistake on purpose. This indicates that CA1 encodes for different information manifolds that can be used differentially depending on the context and behavioral purpose.

We asked whether dCA1 pyramidal cells represent the stimulus identity (HEP vs. MO for odorant identity) or its valence (is this the rewarded stimulus?, S+ vs. S-). We found that prediction of the stimulus decoded from zΔF/F ensemble neural activity in dCA1 was biased towards the unrewarded stimulus (S-) between trials (Figure 7D). This is unlike stimulus identity decoding in areas such as auditory cortex where there is no bias in stimulus prediction (Libby and Buschman, 2021) suggesting that dCA1 ensemble activity represents stimulus value (S+ vs. S-) as opposed to odorant identity (HEP vs. MO). Indeed, when the stimuli were reversed the responses were consistent with

representation of valence for a large portion of the ROIs (Figure 5). This is consistent with valence representation found in olfactory bulb single units after reversal in the go-no go learning task (Doucette and Restrepo, 2008; Li et al., 2015), functional plasticity of sensory inputs elicited by learning in the olfactory bulb (Abraham et al., 2014; Chu et al., 2016), and with decoding of stimulus identity after stimulus reversal for measurements of theta-referenced beta and gamma LFP power in dCA1 (Ramirez-Gordillo *et al.*, 2022). Thus, pyramidal cells represent both odorant valence and odorant identity.

Time-tiled odorant responses in by “time-cells” in dCA1 are thought to be involved in delayed match/non match to sample where they presumably provide short term working memory of the identity of the first odorant that is presented in the task (MacDonald *et al.*, 2013; Taxidis *et al.*, 2020). Interestingly, we find that for the go-no go task the divergence between S+ and S- stimuli in zΔF/F odorant responses of individual pyramidal cells takes place at different times between trial start and reinforcement (Figure 4) and, consistent with these results, stimulus decoding accuracy decoded from single neuron activity starts diverging from accuracy computed from shuffled stimulus labels (50%) at discrete times ranging from trial start to several seconds after reinforcement (Figures 8, S10 and S11). Therefore, decision making for the difference between stimuli based on single cell dCA1 neural activity takes place at different discrete times in dCA1. This finding of what we call “decision-making time-cells” is novel and complementary to stimulus time-cells engaged in delayed match/non match to sample tasks (MacDonald *et al.*, 2013; Taxidis *et al.*, 2020). We hypothesize that this

discrete time tiling of information for decision making in dCA1 by sequential neural dynamics plays a role in go-no go associative learning by representing a memory of whether the rewarded odorant is presented to the animal that the mouse uses to decide whether it should sustain licking to get a reward. Whether this is the case will be determined in future studies.

Finally, our data raise the question on what the specific role is for sequential activity in associative learning in dCA1. On one hand, sequential activity in dCA1 is often associated with transition in the state space where each state encodes for a predictive representation of future states given the current state (Nieh *et al.*, 2021; Stachenfeld et al., 2017). Under this interpretation, time-tiling represents state transition in a cognitive map representing the temporal task structure. On the other hand, sequential activity potentially encodes a single working memory that makes the animal more likely to choose a certain outcome as time passes. Previous modeling work revealed that depending on the model configuration, a recurrent neural network learns to represent working memory either by sequential or persistent activity (Orhan and Ma, 2019). It indicates that time-tiling might be encoding a binary decision (go or no-go) with spatial-temporal patterns. Sequential working memory representation is also beneficial for binding multiple information, such as stimulus identity, valence, and context, into a single working memory (Feldman, 2013; Hiratani and Sompolinsky, 2023). Future work will make it clear whether time-tiling in the decision period represents a transition in the cognitive map or a go/no-go decision variable.

ACKNOWLEDGEMENTS

We would like to thank Brooke Baxter for technical help and Kira Steinke for discussions and feedback on the manuscript. This research was supported by the US National Institutes of Health (NIH UF1 NS116241 and NIH R01 DC000566), and the National Science Foundation (NSF BCS-1926676).

CONTRIBUTIONS

M.M., F.S.de S., E.G. and D.R. conceived and designed the experiments, F.S.de S. performed the surgeries, acquired experimental data and did data analysis, M.M. performed experiments and data analysis, E.G. and G.F. designed and implemented optical instrumentation, G.F. provided technical assistance with multiphoton microscopy, S.A. and D. T. performed sound recordings and analysis, J.R. assisted with immunohistochemistry, A.G.-P. provided technical help, generated illustrations and did immunohistochemistry, J.P. generated code for NWB data sharing, N.H. provided advice on data analysis and writing, M.M., F.S.de S. and D.R. wrote the manuscript and all authors edited the manuscript.

DECLARATION OF INTERESTS

The authors declare no competing interests

STAR * METHODS

Key resources table

REAGENT or RESOURCE	SOURCE	IDENTIFIER
Antibodies		
Donkey anti-rabbit 594 secondary antibody	Jackson Immunoresearch	11-585-152
Rabbit anti GFAP antibody	Abcam	ab7260
EXPERIMENTAL MODELS: ORGANISMS/STRAINS		
Thy1-GCaMP6f mouse, C57BL/6J-Tg(Thy1-GCaMP6f)GP5.17Dkim/J	The Jackson Laboratory	025393
SOFTWARE AND ALGORITHMS		
Demixed PCA	(Kobak *et al.*, 2016)	http://github.com/machenslab/dPCA
Matlab 2022b and 2023a	https://www.mathworks.com/products/matlab.html	N/A
OTHER		
GRIN lenses	GRINTECH GmbH	NEM-050-25-10-860-DS
Metabond	Thermo Fisher	NC0877382, NC2048900, NC2048904
Paraformaldehyde	Electron Microscopy Sciences	15714-S
DAPI	Thermo Fisher	62248
Buprenorphine SR/ER	Zoopharm/Wedgewood	
Vetbond	MWI	006245
Light mineral oil	Fisher	O121-1
Heptanal	Sigma-Aldrich	H-6129
OCT	Sakura Finetech	4583

780 **Animals**

781 All experimental protocols were approved by the Institutional Animal Care and Use
782 Committee of the University of Colorado Anschutz Medical Campus, in accordance to
783 NIH guidelines. Mice were bred in the animal facility and we used both males and
784 females, a total of four adult Thy1-GCaMP6f mouse (Jax 025393 C57BL/6J-Tg(Thy1-
785 GCaMP6f)GP5.17Dkim/J) for head-fixed awake behaving two photon imaging of CA1
786 pyramidal cells through a GRIN lens. We used the 5.17 strain of Thy1-GCaMP6f mice
787 because of their strong expression of GCaMP6f in CA1(Dana et al., 2014). The animals
788 were housed in a vivarium with a 14/10 h light/dark cycle. Food was available ad libitum.
789 Access to water was restricted in behavioral training session according to protocols, all
790 mice were weighed daily and received sufficient water during behavioral sessions to
791 maintain >80% of original body weight.

792

793 **Surgical Procedures**

794 Mice were injected with carprofen (5 mg/kg, IP) one hour prior to surgery and were
795 anesthetized with ketamine/xylazine (IP, 100 mg/kg and 10 mg/kg, respectively).
796 Anesthetic redosing was assessed by pinching the hind feet every 5 min. A craniotomy
797 of diameter ~1.2 mm was made over the right hippocampus and a GRIN lens of 4 mm
798 length and 1 mm diameter (GRINTECH, NEM-050-25-10-860-DS) was implanted at 1.8
799 mm lateral and 2.4 mm caudal of Bregma and 1.25 mm below dura (Radvansky and
800 Dombeck, 2018). The GRIN lens edges were sealed with Vetbond glue (3M, USA) and
801 a custom-made steel head bracket was glued to the skull with Metabond (Parker, USA)
802 for head-fixing and imaging. The mice were treated with buprenorphine SR/ER for two

803 days after surgery (0.05 mg/kg, SQ). dCA1 imaging was initiated two weeks after
804 surgery.
805
806 **Immunohistochemistry and CT-Scan**
807 To visualize GCaMP6f expression in hippocampus CA1 region and GRIN lens track,
808 immunohistochemistry was performed after animals finished all the training. Mice were
809 sacrificed and transcardially perfused with ice cold 4% paraformaldehyde (PFA),
810 followed by equilibration in 30% sucrose. After the brain sank, the tissue was embedded
811 in optimal cutting temperature (OCT) compound and were frozen at -80°C. Slices of 60
812 μm thickness were cut with a Leica cryostat. The slices were stained with rabbit anti-
813 GFAP primary antibody (Ab7260, Abcam, USA) and Alexa Fluor 594 donkey anti-rabbit
814 secondary antibody (11-585-152, Jackson Immunoresearch, USA). The slices were
815 counterstained with DAPI (Thermo Fisher Scientific, USA) and imaged using a confocal
816 laser scanning microscope (Nikon A1R, Japan). To further verify the 3D position of the
817 GRIN lens on the skull and in the brain, we performed microCT-Scan recording. We
818 perfused the mice with PBS and the ex-vivo PFA fixed head was used for acquiring the
819 microCT imaging on a Siemens Inveon microCT system (Siemens, Germany).
820
821 **Go-No Go training**
822 Mice were water deprived by restricting daily consumption of water to 1-1.5 ml. Mice were
823 monitored for signs of dehydration or a decrease in body weight below 80% of the initial
824 weight. If either condition occurred the animals received water ad-lib until they recovered.
825 When the animals were water-deprived, they were trained in a head-fixed olfactory go-no

826 go task with 1% HEP vs MO odorant application (Sigma-Aldrich, USA)(Gire et al., 2013;
827 Li *et al.*, 2015; Ma *et al.*, 2020). Licks were monitored by an electrical circuit monitoring
828 the resistance between the lick spout and recorded with Intan RHD2000 software (Intan,
829 USA). The floor in an olfactometer that controlled valves to deliver a 1:40 dilution of
830 odorant at a rate of 2 L min^{-1}. Lick rate was calculated from the lick records and the time
831 course was convolved with a two second Gaussian for the experiments where we
832 performed multiphoton calcium imaging. The water-deprived mice started the trial by
833 licking on the water port. The odorant was delivered after a random time interval ranging
834 from 1 to 1.5 seconds. In S+ trials, the mice needed to lick at least once in two 2 sec lick
835 segments to obtain a reward (0.1 g ml^{-1} sucrose water) (Figure 1A). In S- trials, the mice
836 need to refrain licking one of the two 2 sec segments to avoid a longer inter-trial interval
837 (+ 10 sec). The animal's behavior performance was evaluated in a sliding window of 20
838 trials and the calculated value was assigned to the last trial in the window. Therefore, it
839 estimated the performance in the last 20 trials. The percent correct value represents the
840 percent of trials in which the animal successfully performed appropriate actions
841 (100*(Hits+CRs)/number of trials), and we considered the animal proficient if percent
842 correct performance is above 80%. In reverse go-no go training sessions the S+ and S-
843 odorants were switched after reaching proficient level in forward training.
844
845 **Acoustic recordings of auditory cue at the start of the trial in the go-no go task**
846
847 In addition to the odorant cue the olfactometer emits a click at the start of the trial when
848 one of the two odorant valves opens 1-1.5 sec before odorant onset. Acoustic

recordings of the olfactometer were made using a GRAS 46BH-1 omnidirectional microphone and GRAS 26AC-1 preamplifier with Type 12AA power module, M-Audio Pro interface, and Audacity software. The microphone was positioned to approximate the location of the mouse's head during experiments. Recordings were time-aligned to experimental hardware using a trigger pulse. Recordings were windowed 7 seconds prior to 15 seconds following stimulus offset and separated according to S- or S+ conditions in Matlab. Spectrograms of each stimulus were then generated to identify potential confounding auditory events.

Figures S3B-C show a sound spectrogram of the click recorded with the ultrasound microphone at the location of the mouse's head in the two-photon microscope aligned with opening of the odorant valve. Figure S3D shows that the identity of the odorant valve (S+ vs S-) can be decoded from the sound click using a generalized linear model (GLM) decoding algorithm, albeit with low accuracy (~ 65%) (ranksum test $p<0.05$, 58 trials for decoding stimuli vs. 290 trials for shuffled stimulus decoding).

While this task provides both olfactory and sound sensory inputs the mouse cues on the olfactory stimulus as shown by the fact that percent correct behavior decreases close to 50% when the odor cues are removed while the valve opening (and consequent sound) are not altered (Figure S2E-G, consistent with previous studies with the same olfactometer (Slotnick and Restrepo, 2005)).

871 **Two photon imaging of dorsal hippocampus CA1 activity in animals undergoing**
872 **the Go-No Go task**
873 All the animals were first habituated to the setup to minimize stress during the imaging
874 experiments. All the imaging sessions started at least 10 minutes after mice had been
875 head-fixed. The head fixed two photon imaging system consisted of a movable objective
876 microscope (MOM, Sutter Instrument Company, USA) paired with a 80 MHz, ~100
877 femtosecond laser (Mai-Tai HP DeepSee, Spectra Physics, USA) centered at 920 nm.
878 The MOM was fitted with a single photon epifluorescence eGFP filter path (475 nm
879 excitation/500-550 nm emission) used for initial field targeting followed by switching to the
880 two photon laser scanning path for imaging GCaMP at the depth of the CA1 cell body
881 layer. Either the galvometric laser scanning system or a resonant scanner were driven by
882 SlideBook 6.0 (Intelligent Imaging Innovations, USA). The two photon time lapses were
883 acquired at 395 x 380 pixels using a 0.4 NA/10x air objective (Olympus, Japan) at either
884 5.3 Hz (galvo) or 20 Hz (resonant). On the day of initial imaging, a FOV was selected to
885 image a large number of active hippocampal CA1 neurons through the GRIN lens, and
886 GCaMP6f movies for several sessions (12-40 trials each) were collected each day. After
887 two photon imaging a second image of the vasculature was captured with wide field
888 epifluorescence to reconfirm the field.
889
890
891 **Statistical analysis**
892 Statistical analysis was performed in Matlab R2022b or R2023a (Mathworks, USA).
893 Statistical significance for changes in measured parameters for multiple factors such as

894 learning and odorant identity (S+ vs. S-) was estimated using a generalized linear model
895 (GLM)(Yu et al., 2022) with post-hoc comparisons performed either with a two-sided t
896 test, or a ranksum test, depending on the result of an Anderson-Darling test of normality.
897 Post-hoc tests were corrected for multiple comparisons using the false discovery rate p
898 value (pFDR) (Curran-Everett, 2000). Asterisks in bar graphs specify statistically
899 significant differences (p<pFDR) on post-hoc tests. Not all statistically significant
900 differences are shown with an asterisks because this makes the figures too complicated.
901 All pairwise post-hoc test p values and pFDR are shown in the supplementary tables.
902 Finally, we provide 95% confidence intervals (CIs)(Halsey et al., 2015) estimated by
903 bootstrap analysis of the mean by sampling with replacement 1000 times using the bootci
904 function in MATLAB (shown in the figures as vertical black lines for bar graphs or shade
905 bounding of mean value lines for time courses).
906
907 **Data analysis**
908 Raw imaging data was first surveyed in ImageJ 1.52 (NIH, USA) to exclude image
909 sequences exhibiting axial movement. We did not find evidence of axial movement while
910 the animal was engaged in the go-no go task. The raw imaging data was processed with
911 DeepCAD-RT to denoise time-lapse images (https://github.com/cabooster/DeepCAD-
912 RT)(Li *et al.*, 2023), and then motion corrected with NoRMCorre algorithm (Pnevmatikakis
913 and Giovannucci, 2017). The nonegative fluorescence traces were generated with
914 EXTRACT (https://github.com/schnitzer-lab/EXTRACT-public)(Hakan *et al.*, 2021) with
915 appropriate parameters. After Extract analysis, the ΔF/F traces of the spatial components
916 were sorted and we assigned trial traces to different behavioral events (Hit, CR, Miss and

CR) and aligned them to trial start, odorant onset or reinforcement delivery for further analysis.

Data analysis was performed using custom code in Matlab R2022b or R2023a (https://github.com/restrepd/CaImAnDR). Four mice were trained in 3-6 training sessions per day. Analysis was performed per session classified into either learning stage with percent correct behavior within the 45-65% range (blue in Figure S2, 20 sessions) or proficient stage with percent correct behavior in the 80-100% range (red in Figure S2, 55 sessions). For each ROI we z-scored ΔF/F by dividing by the standard deviation of ΔF/F calculated over the entire session (we call this z scored ΔF/F zΔF/F). Below we describe the different data analysis methods.

Dimensionality

Following Litwin-Kumar et al. (2017) we defined the dimension of the system (dim) with *M* inputs as the square of the sum of the eigenvalues of the covariance matrix of the measured ΔF/F for all ROIs in the FOV divided by the sum of each eigenvalue squared:

$$\dim\left(\frac{\Delta \mathrm{F}}{\mathrm{F}}\right) = \left(\sum_{i=1}^{M} \lambda_{\mathrm{i}}\right)^{2} / \left(\sum_{i=1}^{M} \lambda_{i}^{2}\right) \qquad (1)$$

where λ_i are the eigenvalues of the covariance matrix of ΔF/F computed over the distribution of ΔF/F signals measured in the FOV. If the components of ΔF/F are independent and have the same variance, all the eigenvalues are equal and dim(ΔF/F) = *M*. Conversely, if the ΔF/F components are correlated so that the data points are

939 distributed equally in each dimension of an *m*-dimensional subspace of the full *M*-
940 dimensional space, only *m* eigenvalues will be nonzero and dim(ΔF/F) = *m*.
941
942 *Demixed principal component analysis*
943
944 Demixed principal component analysis (dPCA) is a dimensionality reduction method
945 decomposing population activity into components related to task parameters such as
946 stimuli, decisions, or rewards (Kobak *et al.*, 2016). dPCA was calculated for S+ or S-
947 trials using code provided by Kobak et al. modified to yield stimulus and independent
948 components using data from all ROIs from all sessions belonging to either the learning or
949 proficient stages.
950
951 *Divergent cell detection and analysis*
952
953 Whether a cell's zΔF/F diverged between S+ and S- (Figures 4 and 5) was determined
954 as follows: Only sessions that included a minimum of 12 trials were included. ROIs with
955 calcium spikes in fewer than 25% of the trials were excluded. For the rest of the ROIs the
956 zΔF/F in the session was considered to be divergent if the GLM p value for S+ vs. S- was
957 below the pFDR. The time for divergence was calculated as the time after trial onset when
958 the S+ and S- 95% CIs did not overlap. Examples of the time course zΔF/F for divergent
959 ROIs are shown in Figure S6A.
960

As shown in Figures 4A, 5A and B and S8A the per trial time courses for z∆F/F were heterogeneous. In order to quantify the heterogeneity we calculated within trial cross correlation coefficients between all divergent z∆F/F time courses (including both S+ and S- in the calculation) for all divergent ROIs (e.g. Figure 4B). The z∆F/F time courses for the different ROIs were then separated into different clusters by estimating an agglomerative hierarchical cluster tree using the linkage function of MATLAB. The number of clusters was specified arbitrarily.

In order to quantify the divergence in z∆F/F between HEP and MO trials for Figure S8 we calculated d', which is a measure of the difference in between two distributions.

$$\mathrm{d}' = \frac{\mathrm{mean}(z\Delta\mathrm{F/F(HEP)}) - \mathrm{mean}(z\Delta\mathrm{F/F(MO)})}{\sqrt{(SD(z\Delta\mathrm{F/F(HEP)})^2 + SD(z\Delta\mathrm{F/F(MO)})^2)/2}} \qquad (2)$$

where SD is the standard deviation. As done for z∆F/F time courses we used cross correlation coefficients and an agglomerative hierarchical cluster tree to sort the time courses shown for d' in Figure S8C,D.

Stimulus decoding

Stimulus decoding was performed using GLM (fitglm in MATLAB). The algorithm was trained per session for all time points and all trials within time periods and number of ROIs per session indicated in the text. Only sessions with 16 or more trials were processed. The predicted stimulus was assessed using leave one trial out and winner takes all procedures. We report the results of GLM decoding, but we obtained similar

983 results with linear discriminant analysis, artificial neural network decoding, binary
984 decision tree decoding and support vector machine decoding (Figure S9).
985 For GLM stimulus decoding performed with a subset of 2, 5 or 15 ROIs (Figure 8)
986 decoding was performed in separate runs with 40 unique subsets of ROIs drawn at
987 random from the total number of ROIs per session.
988
989 *Lick fraction decoding*
990 Lick fraction decoding was performed using a neural network classification model
991 (fitcnet in MATLAB). The algorithm was trained per session for one second windows
992 covering from -5 to + 10 sec in each trial. Only sessions with 16 or more trials were
993 processed. The predicted stimulus was assessed using leave one trial out and winner
994 takes all procedures.
995
996 *Analysis of replay of S+ prediction for stimulus decoding between trials*
997 Sudden changes in stimulus prediction from S- to S+ between trials were determined in
998 decoding prediction moving window averages (with windows of 10 time points) such as
999 the prediction time course shown in Figure 7A. We searched for a replay (arrow in
1000 Figure 7A) by searching for a sudden shift in prediction from below the 5 percentile of
1001 the shuffled stimulus control for decoding prediction (lower edge of the blue shade in
1002 Figure 7A) to above 95 percentile for the shuffled stimulus decoding prediction (upper
1003 edge of the blue shade in Figure 7A). We compared the average time courses for these
1004 sudden between trial increase to S+ (blue line in Figure 7E) to the time course of

decoding prediction centered in the middle of adjacent between trial intervals where we did not find a sudden increase to S+ (magenta line in Figure 7E).

REFERENCES

Abraham, N.M., Vincis, R., Lagier, S., Rodriguez, I., and Carleton, A. (2014). Long term functional plasticity of sensory inputs mediated by olfactory learning. Elife *3*, e02109. 10.7554/eLife.02109.

Aronov, D., Nevers, R., and Tank, D.W. (2017). Mapping of a non-spatial dimension by the hippocampal–entorhinal circuit. Nature *543*, 719-722. 10.1038/nature21692.

Basu, J., and Siegelbaum, S.A. (2015). The corticohippocampal circuit, synaptic plasticity, and memory. Cold Spring Harbor perspectives in biology *7*, a021733.

Biane, J.S., Ladow, M.A., Stefanini, F., Boddu, S.P., Fan, A., Hassan, S., Dundar, N., Apodaca-Montano, D.L., Zhou, L.Z., Fayner, V., et al. (2023). Neural dynamics underlying associative learning in the dorsal and ventral hippocampus. Nature Neuroscience *26*, 798-809. 10.1038/s41593-023-01296-6.

Buzsáki, G., and Llinás, R. (2017). Space and time in the brain. Science *358*, 482-485. 10.1126/science.aan8869.

Buzsaki, G., and Moser, E.I. (2013). Memory, navigation and theta rhythm in the hippocampal-entorhinal system. Nat Neurosci *16*, 130-138. 10.1038/nn.3304.

Cajal, S. (1901). Estudios sobre la corteza cerebral humana. IV. Estructura de la corteza cerebral olfativa del hombre y mamíferos. Trab Lab Invest Biol 1:1-140.

Chu, M.W., Li, W.L., and Komiyama, T. (2016). Balancing the Robustness and Efficiency of Odor Representations during Learning. Neuron *92*, 174-186. 10.1016/j.neuron.2016.09.004.

Citri, A., and Malenka, R.C. (2008). Synaptic plasticity: multiple forms, functions, and mechanisms. Neuropsychopharmacology *33*, 18-41. 10.1038/sj.npp.1301559.

Curran-Everett, D. (2000). Multiple comparisons: philosophies and illustrations. Am.J.Physiol Regul.Integr.Comp Physiol *279*, R1-R8.

Dana, H., Chen, T.-W., Hu, A., Shields, B.C., Guo, C., Looger, L.L., Kim, D.S., and Svoboda, K. (2014). Thy1-GCaMP6 Transgenic Mice for Neuronal Population Imaging In Vivo. PLOS ONE *9*, e108697. 10.1371/journal.pone.0108697.

Doucette, W., and Restrepo, D. (2008). Profound context-dependent plasticity of mitral cell responses in olfactory bulb. PLoS Biol *6*, e258. 08-PLBI-RA-1962 [pii] 10.1371/journal.pbio.0060258.

Edelman, S. (1998). Representation is representation of similarities. Behavioral and Brain Sciences *21*, 449-467. 10.1017/S0140525X98001253.

Eichenbaum, H. (2017). On the Integration of Space, Time, and Memory. Neuron *95*, 1007-1018. 10.1016/j.neuron.2017.06.036.

Fanselow, M.S., and Dong, H.-W. (2010). Are the Dorsal and Ventral Hippocampus Functionally Distinct Structures? Neuron *65*, 7-19. 10.1016/j.neuron.2009.11.031.

Feldman, J. (2013). The neural binding problem(s). Cognitive Neurodynamics *7*, 1-11. 10.1007/s11571-012-9219-8.

Gire, D.H., Whitesell, J.D., Doucette, W., and Restrepo, D. (2013). Information for decision-making and stimulus identification is multiplexed in sensory cortex. Nat Neurosci *16*, 991-993. 10.1038/nn.3432.

Gruart, A., Leal-Campanario, R., Lopez-Ramos, J.C., and Delgado-Garcia, J.M. (2015). Functional basis of associative learning and their relationships with long-term potentiation evoked in the involved neural circuits: Lessons from studies in behaving mammals. Neurobiol Learn Mem *124*, 3-18. 10.1016/j.nlm.2015.04.006.

Hakan, I., Claudia, S., Tugce, T., Biafra, O.A., Oscar, H., Jérôme, L., Fatih, D., Mark, J.W., Murat, A.E., and Mark, J.S. (2021). Fast and statistically robust cell extraction from large-scale neural calcium imaging datasets. bioRxiv, 2021.2003.2024.436279. 10.1101/2021.03.24.436279.

Halsey, L.G., Curran-Everett, D., Vowler, S.L., and Drummond, G.B. (2015). The fickle P value generates irreproducible results. Nature methods *12*, 179-185. 10.1038/nmeth.3288.

Hiratani, N., and Sompolinsky, H. (2023). Optimal quadratic binding for relational reasoning in vector symbolic neural architectures. Neural Computation *35*, 105-155.

Igarashi, K.M., Lu, L., Colgin, L.L., Moser, M.-B., and Moser, E.I. (2014). Coordination of entorhinal–hippocampal ensemble activity during associative learning. Nature *510*, 143-147. 10.1038/nature13162.

Imai, T. (2014). Construction of functional neuronal circuitry in the olfactory bulb. Seminars in Cell & Developmental Biology *35*, 180-188. https://doi.org/10.1016/j.semcdb.2014.07.012.

Kobak, D., Brendel, W., Constantinidis, C., Feierstein, C.E., Kepecs, A., Mainen, Z.F., Qi, X.L., Romo, R., Uchida, N., and Machens, C.K. (2016). Demixed principal component analysis of neural population data. Elife *5*. 10.7554/eLife.10989.

Li, A., Gire, D.H., and Restrepo, D. (2015). Y spike-field coherence in a population of olfactory bulb neurons differentiates between odors irrespective of associated outcome. J Neurosci *35*, 5808-5822. 10.1523/JNEUROSCI.4003-14.2015.

Li, X., Li, Y., Zhou, Y., Wu, J., Zhao, Z., Fan, J., Deng, F., Wu, Z., Xiao, G., He, J., et al. (2023). Real-time denoising enables high-sensitivity fluorescence time-lapse imaging beyond the shot-noise limit. Nature Biotechnology *41*, 282-292. 10.1038/s41587-022-01450-8.

Li, Y., Xu, J., Liu, Y., Zhu, J., Liu, N., Zeng, W., Huang, N., Rasch, M.J., Jiang, H., Gu, X., et al. (2017). A distinct entorhinal cortex to hippocampal CA1 direct circuit for olfactory associative learning. Nature Neuroscience *20*, 559-570. 10.1038/nn.4517.

Libby, A., and Buschman, T.J. (2021). Rotational dynamics reduce interference between sensory and memory representations. Nature Neuroscience *24*, 715-726. 10.1038/s41593-021-00821-9.

Litwin-Kumar, A., Harris, K.D., Axel, R., Sompolinsky, H., and Abbott, L.F. (2017). Optimal Degrees of Synaptic Connectivity. Neuron *93*, 1153-1164 e1157. 10.1016/j.neuron.2017.01.030.

Ma, M., Futia, G.L., de Souza, F.M.S., Ozbay, B.N., Llano, I., Gibson, E.A., and Restrepo, D. (2020). Molecular layer interneurons in the cerebellum encode for valence in associative learning. Nature Communications *11*, 4217. 10.1038/s41467-020-18034-2.

MacDonald, C.J., Carrow, S., Place, R., and Eichenbaum, H. (2013). Distinct Hippocampal Time Cell Sequences Represent Odor Memories in Immobilized Rats. The Journal of Neuroscience *33*, 14607. 10.1523/JNEUROSCI.1537-13.2013.

Manns, J.R., Zilli, E.A., Ong, K.C., Hasselmo, M.E., and Eichenbaum, H. (2007). Hippocampal CA1 spiking during encoding and retrieval: relation to theta phase. Neurobiol Learn Mem *87*, 9-20. 10.1016/j.nlm.2006.05.007.

Martin, C., Beshel, J., and Kay, L.M. (2007). An olfacto-hippocampal network is dynamically involved in odor-discrimination learning. J.Neurophysiol. *98*, 2196-2205.

Martinez, R.H., Lansner, A., and Herman, P. (2019). Probabilistic associative learning suffices for learning the temporal structure of multiple sequences. PLOS ONE *14*, e0220161. 10.1371/journal.pone.0220161.

Mau, W., Sullivan, D.W., Kinsky, N.R., Hasselmo, M.E., Howard, M.W., and Eichenbaum, H. (2018). The Same Hippocampal CA1 Population Simultaneously Codes Temporal Information over Multiple Timescales. Current Biology *28*, 1499-1508.e1494. https://doi.org/10.1016/j.cub.2018.03.051.

Michon, F., Sun, J.-J., Kim, C.Y., Ciliberti, D., and Kloosterman, F. (2019). Post-learning Hippocampal Replay Selectively Reinforces Spatial Memory for Highly Rewarded

Locations. Current Biology *29*, 1436-1444.e1435. https://doi.org/10.1016/j.cub.2019.03.048.

Moser, E., Moser, M.B., and Andersen, P. (1993). Spatial learning impairment parallels the magnitude of dorsal hippocampal lesions, but is hardly present following ventral lesions. The Journal of Neuroscience *13*, 3916. 10.1523/JNEUROSCI.13-09-03916.1993.

Neves, G., Cooke, S.F., and Bliss, T.V.P. (2008). Synaptic plasticity, memory and the hippocampus: a neural network approach to causality. Nature Reviews Neuroscience *9*, 65-75. 10.1038/nrn2303.

Nieh, E.H., Schottdorf, M., Freeman, N.W., Low, R.J., Lewallen, S., Koay, S.A., Pinto, L., Gauthier, J.L., Brody, C.D., and Tank, D.W. (2021). Geometry of abstract learned knowledge in the hippocampus. Nature *595*, 80-84. 10.1038/s41586-021-03652-7.

Orhan, A.E., and Ma, W.J. (2019). A diverse range of factors affect the nature of neural representations underlying short-term memory. Nature Neuroscience *22*, 275-283. 10.1038/s41593-018-0314-y.

Pnevmatikakis, E.A., and Giovannucci, A. (2017). NoRMCorre: An online algorithm for piecewise rigid motion correction of calcium imaging data. J Neurosci Methods *291*, 83-94. 10.1016/j.jneumeth.2017.07.031.

Radvansky, B.A., and Dombeck, D.A. (2018). An olfactory virtual reality system for mice. Nat Commun *9*, 839. 10.1038/s41467-018-03262-4.

Ramirez-Gordillo, D., Bayer, K.U., and Restrepo, D. (2022). Hippocampal-Prefrontal θ Coupling Develops as Mice Become Proficient in Associative Odorant Discrimination Learning. eneuro *9*, ENEURO.0259-0222.2022. 10.1523/ENEURO.0259-22.2022.

Rangel, L.M., Rueckemann, J.W., Riviere, P.D., Keefe, K.R., Porter, B.S., Heimbuch, I.S., Budlong, C.H., and Eichenbaum, H. (2016). Rhythmic coordination of hippocampal neurons during associative memory processing. Elife *5*. 10.7554/eLife.09849.

Schaper, M. (1993). Development of a database for sensory irritants and its use in establishing occupational exposure limits. Am.Ind.Hyg.Assoc.J. *54*, 488-544.

Shimbo, A., Izawa, E.-I., and Fujisawa, S. Scalable representation of time in the hippocampus. Science Advances *7*, eabd7013. 10.1126/sciadv.abd7013.

Singer, Annabelle C., Carr, Margaret F., Karlsson, Mattias P., and Frank, Loren M. (2013). Hippocampal SWR Activity Predicts Correct Decisions during the Initial Learning of an Alternation Task. Neuron *77*, 1163-1173. https://doi.org/10.1016/j.neuron.2013.01.027.

Singer, W., and Lazar, A. (2016). Does the cerebral cortex exploit high-dimensional, non-linear dynamics for information processing? Frontiers in computational neuroscience *10*, 99.

Slotnick, B.M., and Restrepo, D. (2005). Olfactometry with mice. In Current Protocols in Neuroscience, J.N. Crawley, C.R. Gerefen, M.A. Rogawski, D.R. Sibley, P. Skolnick, and S. Wray, eds. (John Wiley and Sons, Inc), pp. 1-24

Stachenfeld, K.L., Botvinick, M.M., and Gershman, S.J. (2017). The hippocampus as a predictive map. Nature Neuroscience *20*, 1643-1653. 10.1038/nn.4650.

Stefanini, F., Kushnir, L., Jimenez, J.C., Jennings, J.H., Woods, N.I., Stuber, G.D., Kheirbek, M.A., Hen, R., and Fusi, S. (2020). A Distributed Neural Code in the Dentate Gyrus and in CA1. Neuron *107*, 703-716.e704. https://doi.org/10.1016/j.neuron.2020.05.022.

Strange, B.A., Witter, M.P., Lein, E.S., and Moser, E.I. (2014). Functional organization of the hippocampal longitudinal axis. Nature Reviews Neuroscience *15*, 655-669. 10.1038/nrn3785.

Taxidis, J., Pnevmatikakis, E.A., Dorian, C.C., Mylavarapu, A.L., Arora, J.S., Samadian, K.D., Hoffberg, E.A., and Golshani, P. (2020). Differential Emergence and Stability of Sensory and Temporal Representations in Context-Specific Hippocampal Sequences. Neuron *108*, 984-998.e989. https://doi.org/10.1016/j.neuron.2020.08.028.

Wiltgen, B.J., Zhou, M., Cai, Y., Balaji, J., Karlsson, M.G., Parivash, S.N., Li, W., and Silva, A.J. (2010). The Hippocampus Plays a Selective Role in the Retrieval of Detailed Contextual Memories. Current Biology *20*, 1336-1344. https://doi.org/10.1016/j.cub.2010.06.068.

Witter, M.P., Doan, T.P., Jacobsen, B., Nilssen, E.S., and Ohara, S. (2017). Architecture of the Entorhinal Cortex A Review of Entorhinal Anatomy in Rodents with Some Comparative Notes. Frontiers in Systems Neuroscience *11*.

Wood, E.R., Dudchenko, P.A., and Eichenbaum, H. (1999). The global record of memory in hippocampal neuronal activity. Nature *397*, 613-616. 10.1038/17605.

Yu, Z., Guindani, M., Grieco, S.F., Chen, L., Holmes, T.C., and Xu, X. (2022). Beyond t test and ANOVA: applications of mixed-effects models for more rigorous statistical analysis in neuroscience research. Neuron *110*, 21-35. https://doi.org/10.1016/j.neuron.2021.10.030.

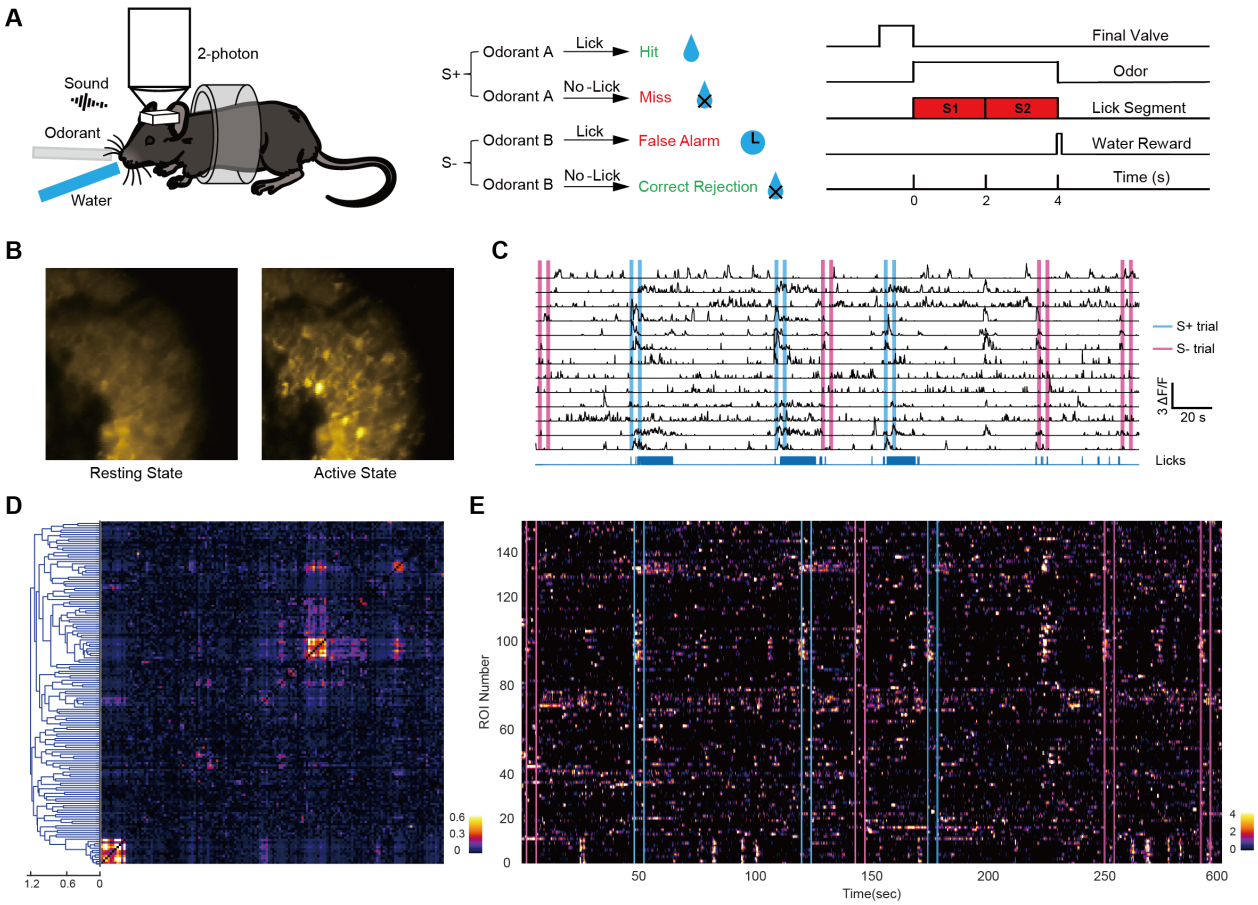

Figure 1. Two-photon Ca^{2+} imaging of pyramidal cells in CA1 in head-fixed mice undergoing the go-no go associative learning task.

(A) Go-no go task. Left: Two-photon imaging of a head-fixed mouse responding to odorants by licking on a water spout in response to the rewarded odorant in the go-no go task. Center: Scoring of decision making. Right: time course for the trial. For water reward in Hit trials the animal must lick at least once in each of the two 2 second lick segments.

(B) Two photon microscopy images of GCaMP6f fluorescence recorded from CA1 pyramidal cells through a GRIN lens in a proficient Thy1-GCaMP6f mouse engaged in

1191 the go-no go task. Left: Activity at rest. Right: Activity during rewarded odorant trial. Video
1192 1 shows fluorescence changes in this group of cells.
1193
1194 (C) ΔF/F traces are shown for a subset of the regions of interest (ROIs) for the figure
1195 shown in B. The magenta vertical lines are the on and off times for the odorant in the
1196 unrewarded (S-) odorant trials and the cyan vertical lines are on and off times for the
1197 rewarded (S+) odorant. The blue lines at the bottom are lick recordings.
1198
1199 (D) Cross correlation and hierarchical clustering of the ΔF/F traces for 153 ROIs for the
1200 entire 20 min session corresponding to B and C shows substantial heterogeneity in the
1201 calcium responses.
1202
1203 (E) Pseudocolor plot of the time course for ΔF/F for the 153 hierarchically clustered ROIs.
1204 Figure S1 shows the time courses for S+ and S- trials for the mean ΔF/F traces, lick
1205 fraction and a p value quantifying the difference between S+ and S- licks.
1206

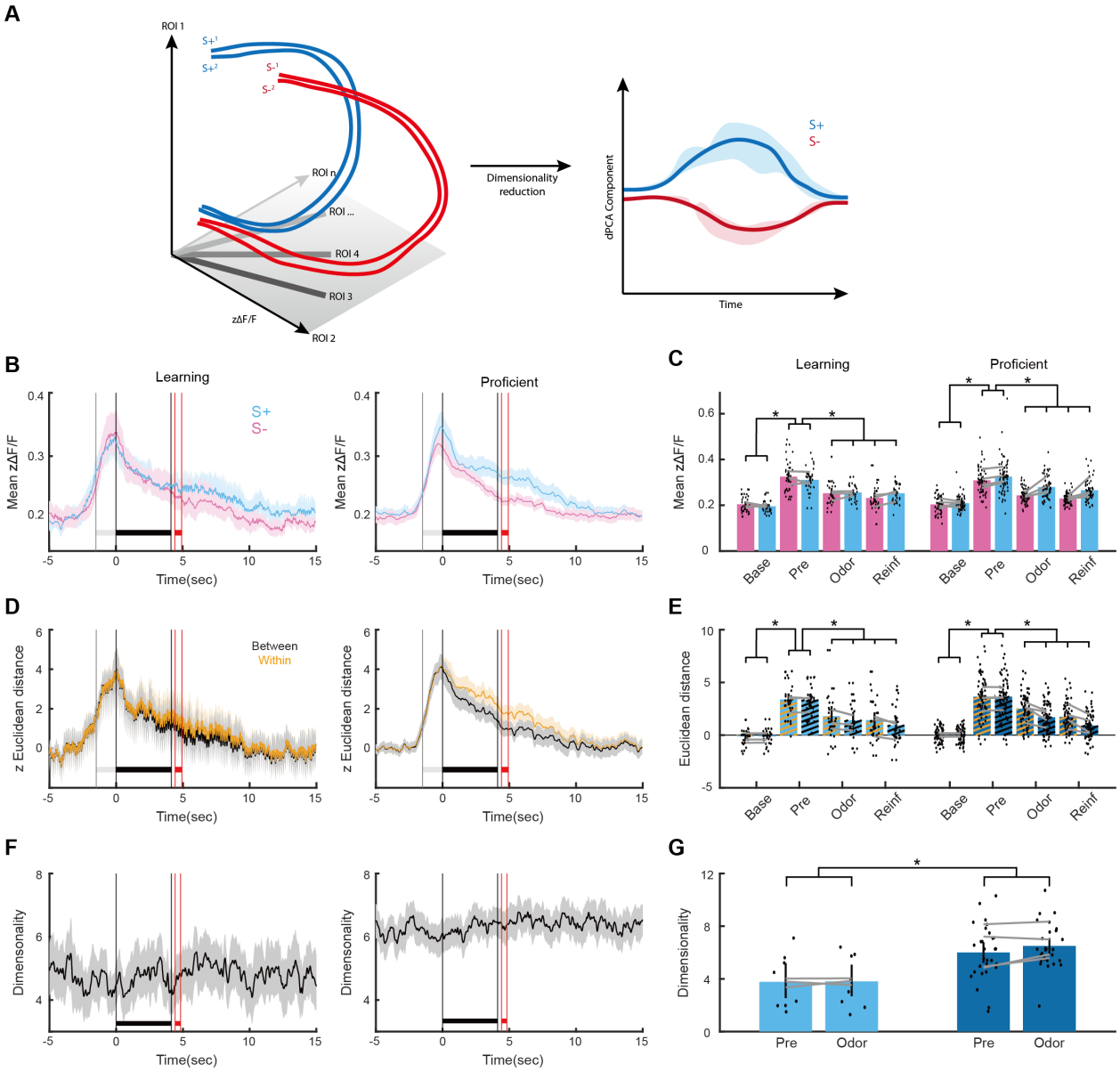

Figure 2. Changes in n-dimensional zΔF/F space start before the animal starts the trial and dimensionality increases with learning.

(A) Diagram illustrating the trajectory for the time course of S+ and S- trials in n-dimensional zΔF/F space and how dimensionality reduction by demixed PCA (dPCA,

Figure 3) reduces the dimensions to stimulus-relevant components. z∆F/F is z-scored ∆F/F (see methods).

(B) Mean of per trial z∆F/F time course for S+ and S- trials for all learning and proficient sessions. Left: learning stage, right: proficient stage.

(C) Bar graph showing the mean value of z∆F/F calculated in the following time windows: Base: -4.5 to -3.5 sec, Pre: -1 to 0 sec, Odor: 3.1 to 4.1 sec, Reinf: 4.5 to 5.5 sec. Dots are z∆F/F values per session and grey lines are z∆F/F values per mouse.

(D) Mean per trial Euclidean distance calculated in n dimensional z∆F/F ROI space. The Euclidean distance was calculated: 1) At each time point for each pair of S+ vs. S- trials and we plot the mean of all of the pair Euclidean distances (we call this “Between” Euclidean distance). 2) At each time point for each pair of S+ vs. S+ or S- vs. S- trials and we plot the mean of all of the pair Euclidean distances (we call this “Within” Euclidean distance).

(E) Bar graph showing the mean value of between and within Euclidean distances calculated in the following time windows: Base: -4.5 to -3.5 sec, Pre: -1 to 0 sec, Odor: 3.1 to 4.1 sec, Reinf: 4.5 to 5.5 sec. Dots are Euclidean distance values per session and grey lines are Euclidean distance values per mouse. Hatch bar colors are the same as the colors for between and within in panel D.

(F) Mean per trial dimensionality calculated in n dimensional zΔF/F ROI space.

(G) Bar graph showing the mean per trial dimensionality calculated in the following time windows: Base: -4.5 to -3.5 sec, Pre: -1 to 0 sec, Odor: 3.1 to 4.1 sec, Reinf: 4.5 to 5.5 sec. Dots are dimensionality values per session and grey lines are dimensionality values per mouse.

GLM statistical analysis and post hoc statistics for significance of differences for the bar graphs are shown in Tables S2 and S3.

For all figures in the manuscript: The bounded lines such as those in B, D and F represent mean and 95% CI. The light grey horizontal bar is the period between the earliest trial start and odorant presentation (at 0 sec), the black horizontal bar is the time period for odorant presentation and the red horizontal bar is the period for water reward delivery.

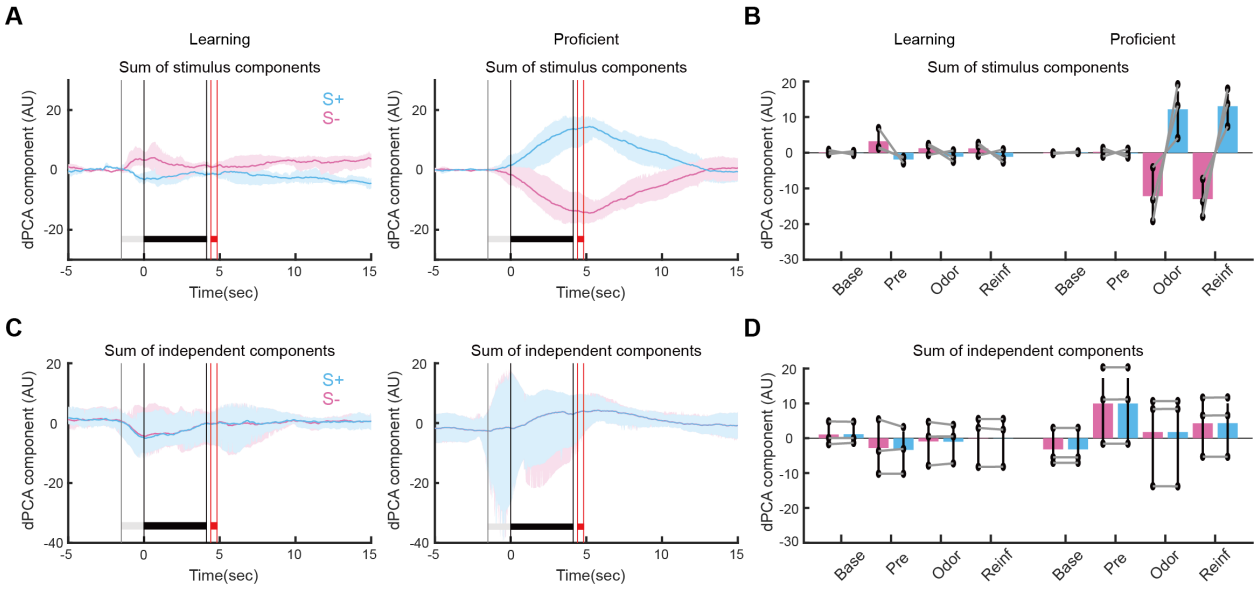

Figure 3. Demixed PCA reveals a substantial increase elicited by learning in the divergence between S+ and S- stimulus components.

(A) Time courses for the sum of demixed PCA (dPCA) stimulus components for the learning (i, 20 sessions, 4 mice) and proficient (ii, 55 sessions, 4 mice) stages.

(B) Bar graph showing the mean value of the sum of stimulus dPCA components calculated in the following time windows: Base: -4.5 to -3.5 sec, Pre: -1 to 0 sec, Odor: 3.1 to 4.1 sec, Reinf: 4.5 to 5.5 sec.

(C) Time courses for the sum of independent dPCA components for the learning (i, 20 sessions, 4 mice) and proficient (ii, 55 sessions, 4 mice) stages.

(D) Bar graph showing the mean value of the sum of independent dPCA components calculated in the same time windows as in (B).

1270

1271 dPCA was performed following the procedure in (Kobak *et al.*, 2016). An example for all

1272 components and dPCA explained variance for one mouse is shown in Figure S5. GLM

1273 statistical analysis and post hoc statistics for significance of differences for the bar graphs

1274 are shown in Table S4.

1275

1276

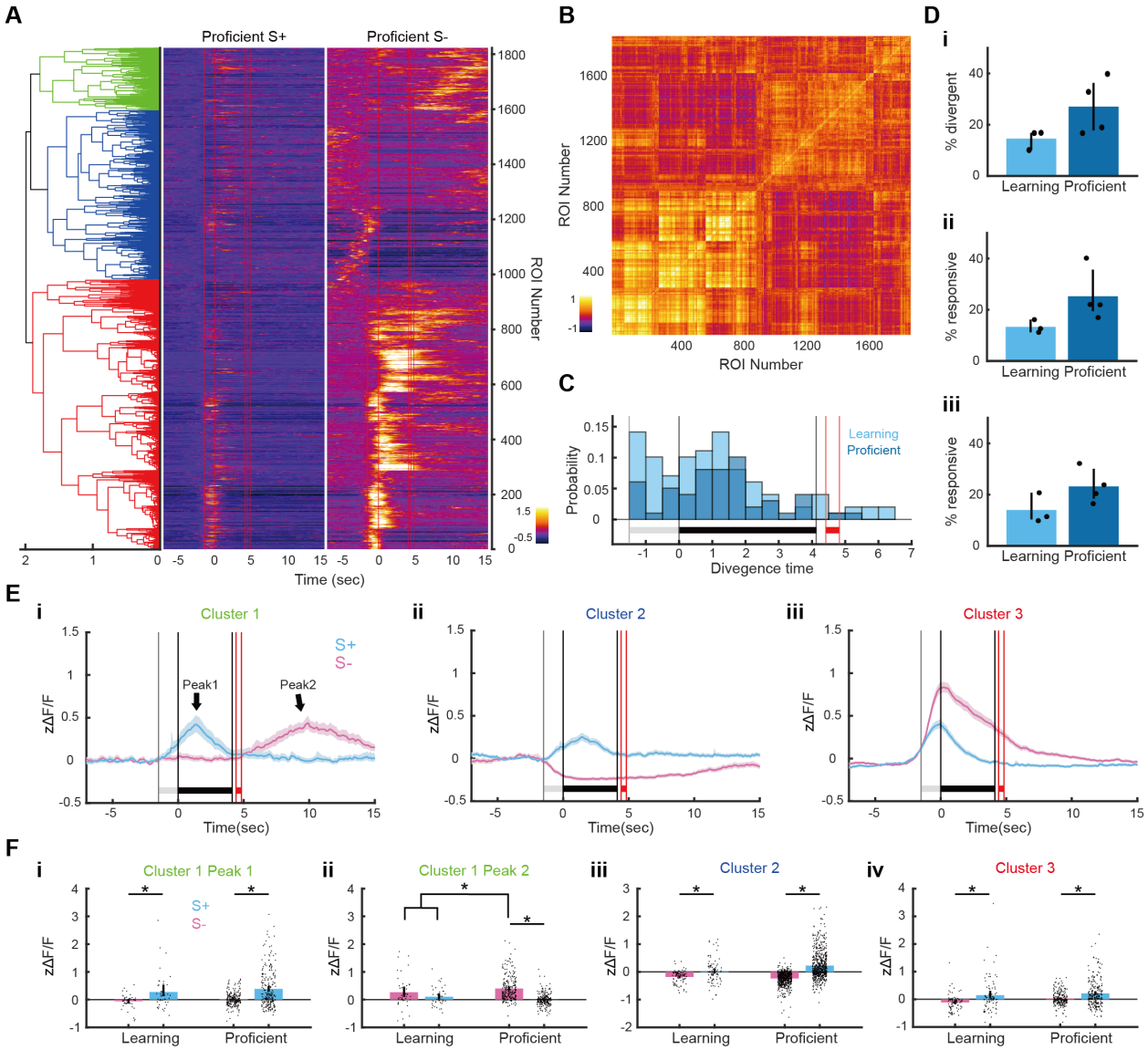

Figure 4. The magnitude of divergence between S+ and S- zΔF/F responses increases with learning and the onset of divergence takes place at discrete times that differ between the learning and proficient stages.

(A) zΔF/F time courses for single ROIs that were divergent between S+ and S- trials in the proficient sessions (66 sessions, 4 mice). Time courses were sorted by estimating an agglomerative hierarchical cluster tree shown on the left that was calculated using the

cross correlation coefficients between all divergent z∆F/F time courses shown in C. The red vertical lines show (in order): trial start, odorant on, odorant off, reinforcement on and reinforcement off.

(B) Cross correlation coefficients computed between all per trial z∆F/F time courses shown in A. The coefficients were sorted by the agglomerative hierarchical cluster tree shown in A.

(C) Histograms for divergence times for all the ROIs for the proficient stage shown in A (dark blue) and for all divergent ROIs for learning stage sessions (20 sessions, light blue). Divergence time histograms are significantly different between learning and proficient (ranksum $p<0.001$, $n=99$ divergence time bins).

(D) i. Percent divergent ROIs per mouse. ii and iii. Percent responsive ROIs per mouse for S+ and S- trials. The percent divergent (i) and percent responsive (ii and ii) differences between learning and proficient stages were not statistically significant (two tailed t test $p>0.05$, $n=3$ for learning and 4 for proficient, 5 d.f.).

(E) Mean z∆F/F time courses for the three clusters in the hierarchical tree shown in A.

(F) Peak z∆F/F calculated per session for each cluster. Note that cluster 1 has two peaks (see arrows in Ei).

1308 Table S5 shows the GLM statistical analysis for Figure 4F.

1309

1310

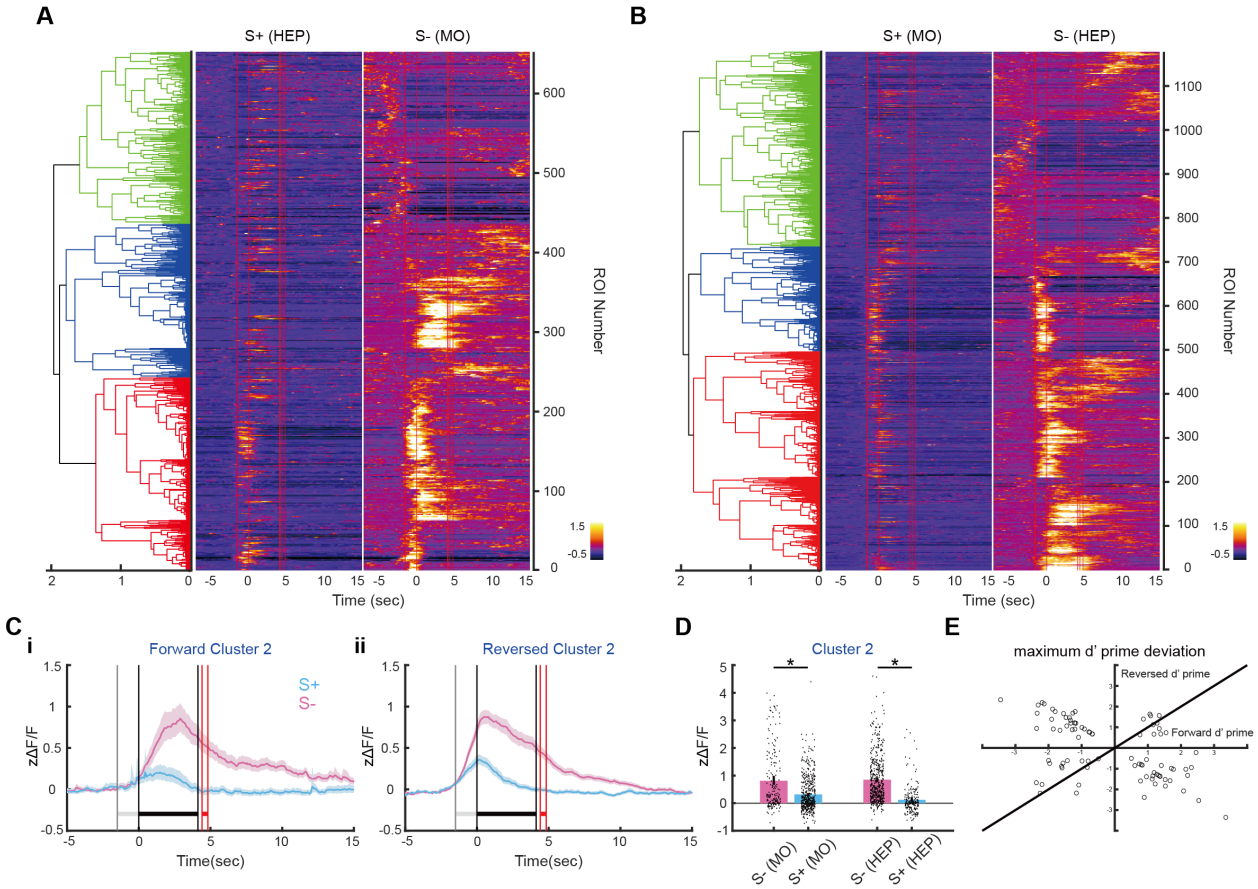

Figure 5. Reversal of odorant valence reveals that a substantial number of dCA1 cells respond to stimulus valence.

(A and B) zΔF/F time courses for single ROIs that were divergent between S+ and S- trials for proficient mice. (A) shows zΔF/F time courses for the forward proficient sessions where the rewarded odorant (S+) was HEP and the unrewarded odorant (S-) was MO (25 sessions, 4 mice) and (B) shows time courses for the reversed proficient sessions where the rewarded odorant (S+) was MO and the unrewarded odorant (S-) was HEP (41 sessions, 4 mice). For both A and B time courses were sorted by estimating an agglomerative hierarchical cluster tree shown on the left that was calculated using the cross correlation coefficients between all divergent zΔF/F time courses shown in Figure

S7 C. The red vertical lines in A and B show (in order): trial start, odorant on, odorant off, reinforcement on and reinforcement off.

(C) Mean z∆F/F time courses for cluster 2 (blue cluster in A and B). Mean z∆F/F time courses for clusters 1 and 3 are shown in Figure S7.

(D) Peak z∆F/F calculated per session for cluster 2. Table S6 shows the GLM statistical analysis for these data.

(E) Relationship for recordings in one mouse between forward and reversed peak d' for HEP vs. MO for all forward stimulus divergent z∆F/F time courses for a set of forward/reversed sessions where ROIs were matched from session to session. The per ROI z∆F/F and d' time courses for these forward and reversed sessions are shown in Figure S8. The line shown is d' reversed = d' forward that would be followed if the ROIs represent stimulus identity.

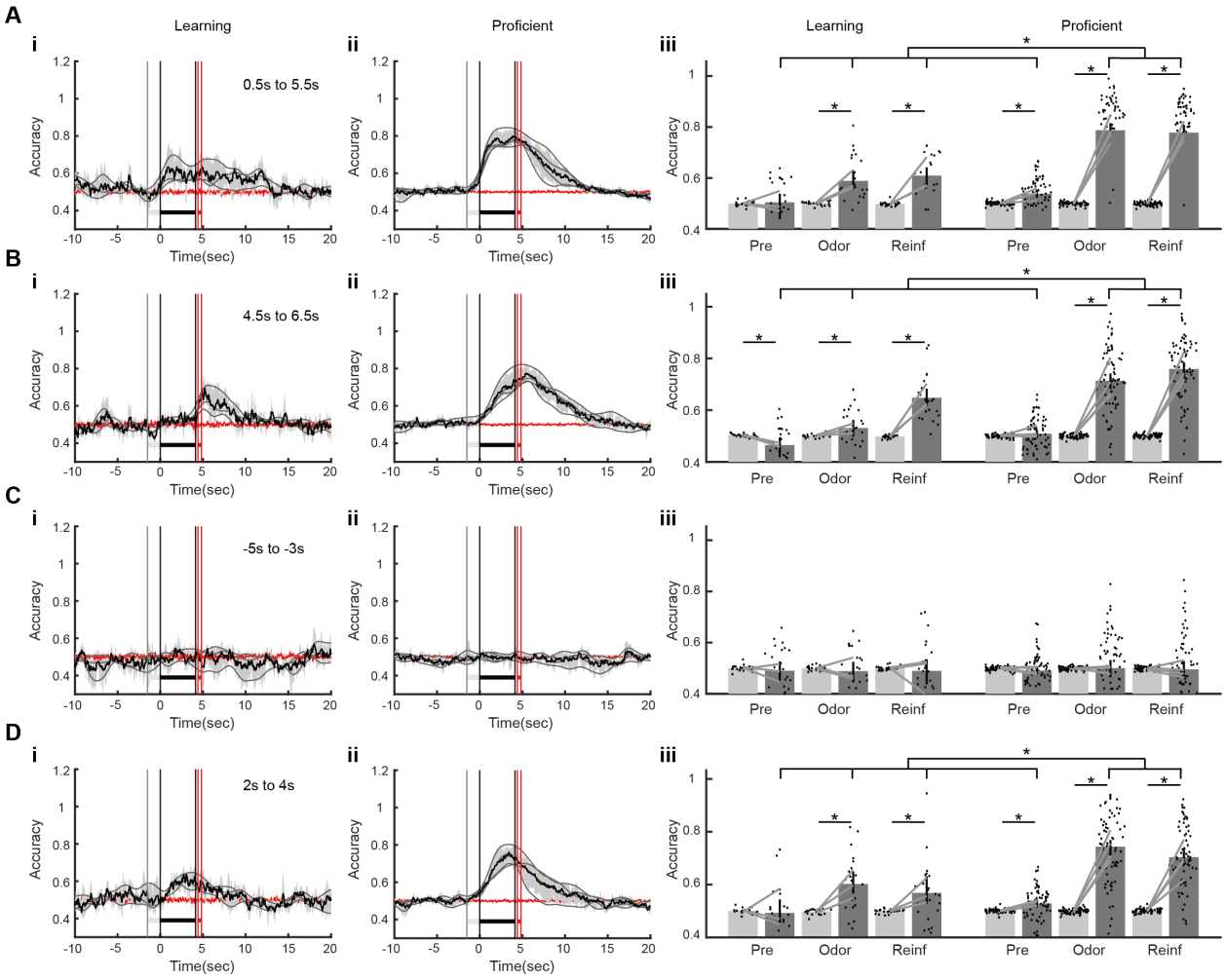

Figure 6. Learning elicits an increase in stimulus decoding accuracy.

(A to D). Each panel shows the accuracy of GLM decoding of the stimulus (S+ vs. S-) from per trial z∆F/F responses for all trials and all ROIs per session for all learning stage sessions (i) and proficient sessions (ii) (4 mice, 18 learning sessions, 66 proficient sessions). The bounded black line represents the mean accuracy bounded by the 95% CI. The grey lines are per mouse accuracies. The red line is the stimulus decoding accuracy calculated after shuffling the stimulus labels (S+ vs S-). A to D differ by the time

period used to train the GLM decoder. The A training period (0.5 to 5.5 sec) covers most of the odorant training period, the B training period takes place before trial onset (-5 to -3 sec), the period for C included the reward delivery period (4.5 to 6.5 sec) and the training period for D was the latter half of the odorant period (2-4 sec). The bar graphs in iii show the mean accuracy for different accuracy periods (Pre -1 to 0, Odor 3.1 to 4.1 and Reinf 4.5 to 5.5). Light gray bars are the shuffled stimulus accuracies. Points are per session accuracies and bars are 95% CIs.

*$p<0.05$ for a pFDR-corrected t-test or ranksum tests, GLM statistics are in Table S7.

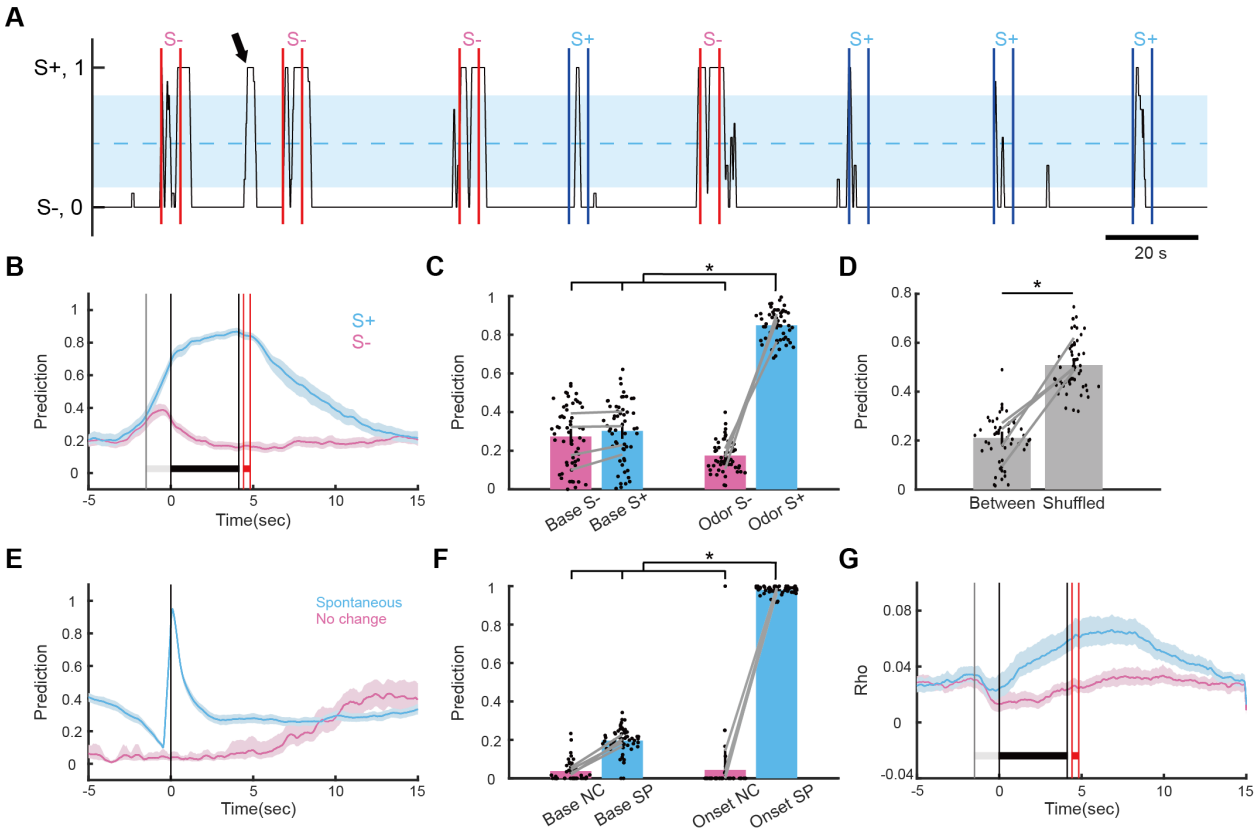

Figure 7. Replay of prediction of S+ for stimulus decoding between trials.

(A) Example of the time course for stimulus decoding prediction during a session when the animal was proficient in the go-no go task. Prediction ranges from 0 (S-) to 1 (S+). Cyan vertical bars are the odor on and odor off times for the S+ trials and magenta vertical bars are the odor on and odor off times for the S- trials. The shaded blue area is the 5 to 95 percentile decoding prediction calculated for decoding with shuffled trial labels. The arrow points to a sudden shift in prediction above shuffled 95 percentile that took place between trials (we call this a replay).

(B) Mean label prediction time course within trials calculated for S+ and S- trials for all sessions when the mice were proficient (66 sessions, 4 mice).

(C) Bar graph quantifying mean label prediction for S+ and S- trials in two time windows: Base (-2.5 to -1.5 sec) and odor (2 to 4.1 sec). Dots are per session mean label prediction and grey lines are per mouse mean label prediction.

(D) Bar graph quantifying the mean label prediction between trials compared to the mean label prediction between trials for shuffled label decoding.

(E) Mean label prediction time course for between trial replays ("replay") and for time courses in between trials periods where we did not find spontaneous shifts to S+ ("no change") (66 sessions, 4 mice).

(F) Bar graph quantifying mean label prediction for between trial spontaneous prediction shifts and for no change between trial prediction time courses calculated in two time windows: Base (-2.5 to -1.5 sec) and odor (2 to 4.1 sec). Dots are per session mean label prediction and grey lines are per mouse mean label prediction.

(G) Correlation between label prediction calculated at each time point in the prediction time course for all S+ or S- trials within a session and the label prediction value found at the point of spontaneous shift for spontaneous shifts in prediction found in between trials in the same session (66 sessions, 4 mice).

*$p<0.05$ for a pFDR-corrected t-test or ranksum tests, GLM statistics are in Table S8.

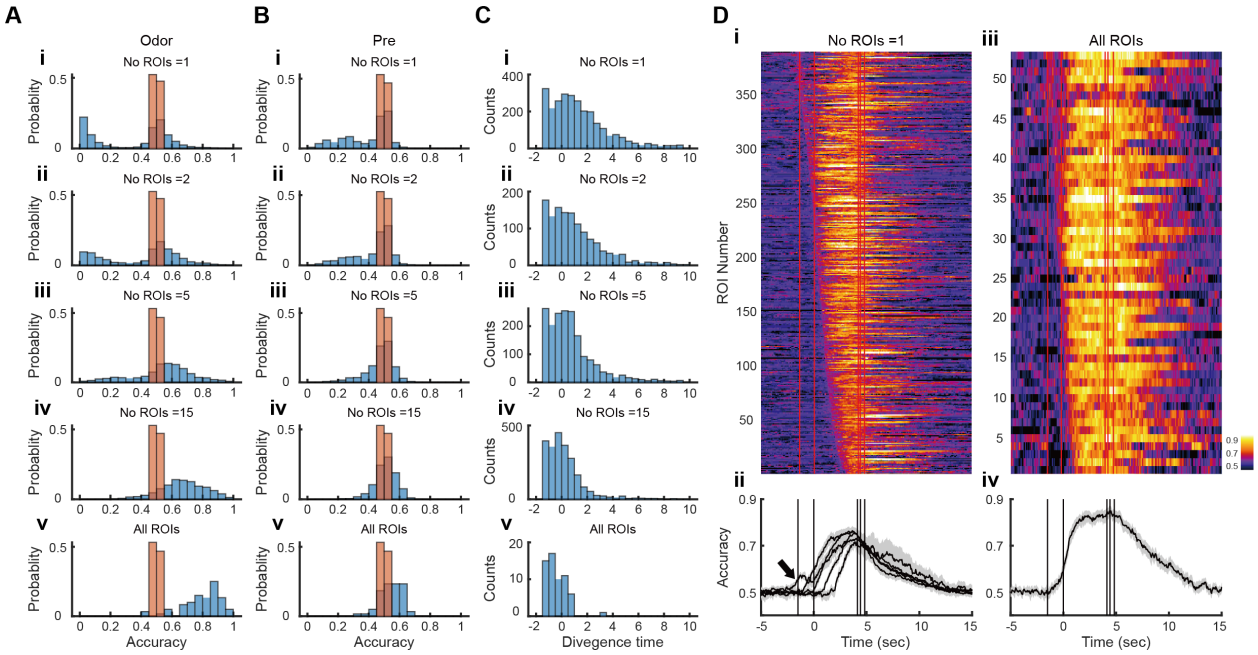

Figure 8. GLM stimulus decoding accuracy calculated with different subsets of ROIs per session reveals time tiling of the onset of the increase in stimulus decoding accuracy.

(A) Histogram for stimulus decoding accuracy calculated in the odor period (3.1 to 4.1 sec) for all proficient sessions (66 sessions) for 4 mice. i to v show the histogram for an increasing number of ROIs per decoding session. Blue is stimulus decoding accuracy, brown is stimulus decoding accuracy calculated after shuffling the labels. Histograms were normalized by dividing by the total number of counts.

(B) Histograms calculated in the Pre period (-1 to 0 sec).

(C) Histograms for the onset of the increase in decoding accuracy for decoding runs that achieved at least 0.65 accuracy after trial start.

(D) (i). Time courses for decoding accuracies calculated with one ROI per session that reach at least 0.65 after trial start. (ii) Mean accuracy time courses calculated for one ROI accuracy time courses shown in Di with accuracy increase onsets in the following time windows: -1.5 to -1, -1 to 0, 0 to 1, 1 to 2, 2 to 3, >3 sec. (iii) Time courses for decoding accuracies calculated all ROIs per session. (iv) Mean accuracy time course for the time courses shown in Diii.

GLM analysis indicates that all histograms in A and B differ from each other and all histograms in C differ from each other (Table S9).

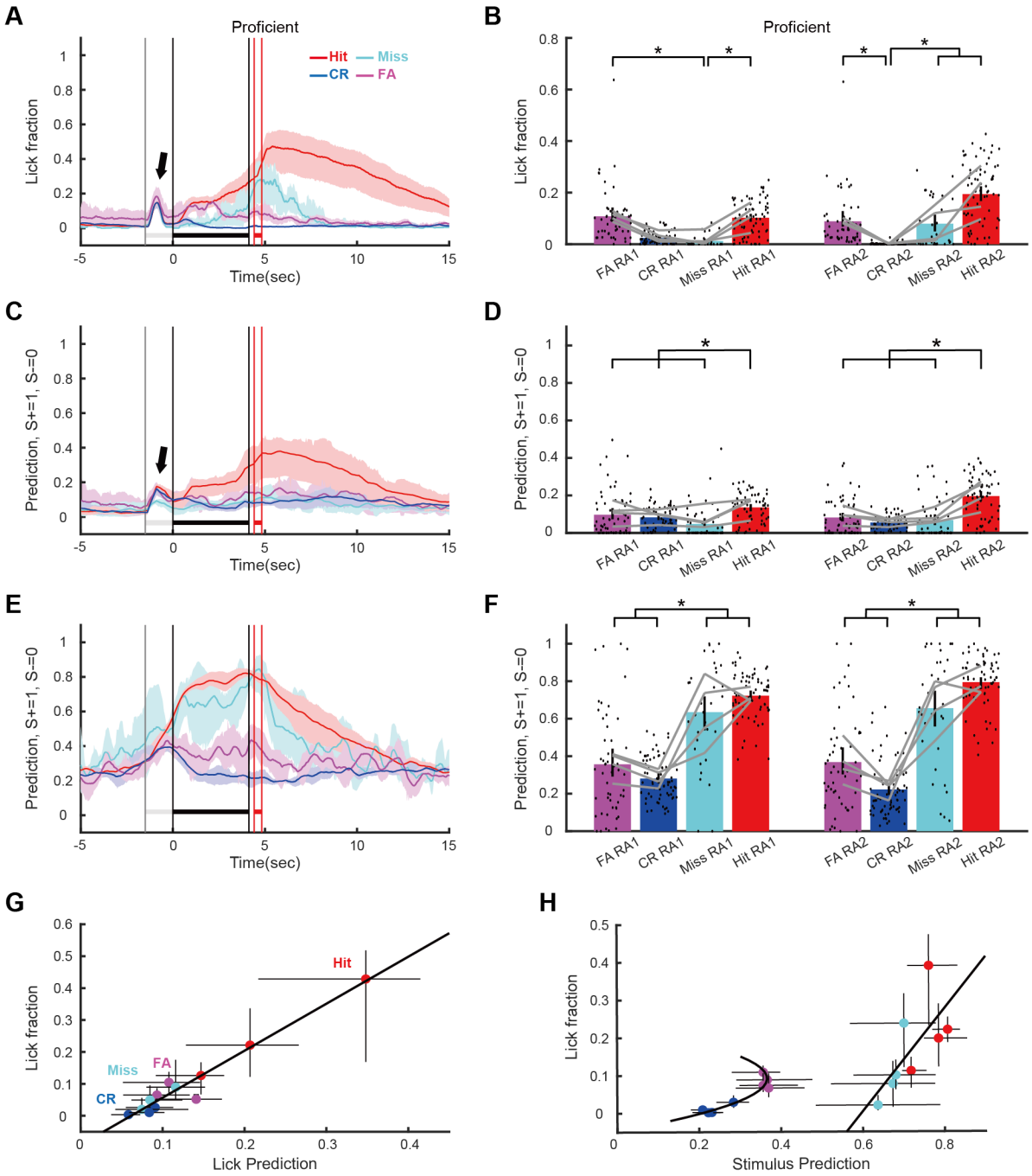

Figure 9. The relationship between lick fraction and prediction differs between stimulus decoding and decoding of lick fraction.

(A) Mean lick fraction time course calculated for hits (red), miss (cyan), correct rejections (CR, blue) or false alarm (FA, magenta) trials for all sessions when the mice were proficient (66 sessions, 4 mice).

(B) Bar graph quantifying mean lick fraction for proficient mice (66 sessions, 4 mice) in the two 2 second response areas of the odor period where the mouse must lick at least once to get water in a Hit trial (Figure 1A). Dots are per session lick fraction and grey lines are per mouse averages.

(C) Mean prediction time course for lick fraction decoding within trials calculated for hits (red), miss (cyan), correct rejections (CR, blue) or false alarm (FA, magenta) trials for all sessions when the mice were proficient (66 sessions, 4 mice).

(D) Bar graph quantifying mean lick fraction prediction for proficient mice (66 sessions, 4 mice) in the two 2 second response areas of the odor period where the mouse must lick at least once to get water in a Hit trial (Figure 1A). Dots are per session prediction and grey lines are per mouse averages.

(E) Mean stimulus prediction time course within trials calculated for hits (red), miss (cyan), correct rejections (CR, blue) or false alarm (FA, magenta) trials for all sessions when the mice were proficient (66 sessions, 4 mice).

(F) Bar graph quantifying mean stimulus prediction for proficient mice (66 sessions, 4 mice) in the two 2 second response areas of the odor period where the mouse must lick at least once to get water in a Hit trial (Figure 1A). Dots are per session prediction and grey lines are per mouse averages. The training period for the GLM decoding algorithm was 0.5 to 5.5 sec.

(G) Relationship between mean lick fraction and mean lick fraction prediction (calculated from per mouse values). The bars are 95% CIs calculated per mouse. Lick fraction and lick fraction prediction were calculated in two second time windows spanning from odor onset to 6 sec after odor onset. The line is a linear fit.

(H) Relationship between mean lick fraction and mean stimulus prediction (calculated from per mouse values). The bars are 95% CIs calculated per mouse. Lick fraction and stimulus prediction were calculated in two second time windows spanning from odor onset to 6 sec after odor onset. The data for Hit and Miss is fit by a linear fit and the data for CR and FA is fit by a second order polynomial.

For all graphs the data are shown separately for S+ Hits (red) and Miss (cyan) and S- CR (blue) and FA (magenta) trials. *$p<0.05$ for a pFDR-corrected t-test or ranksum tests, GLM statistics are in Table S10.

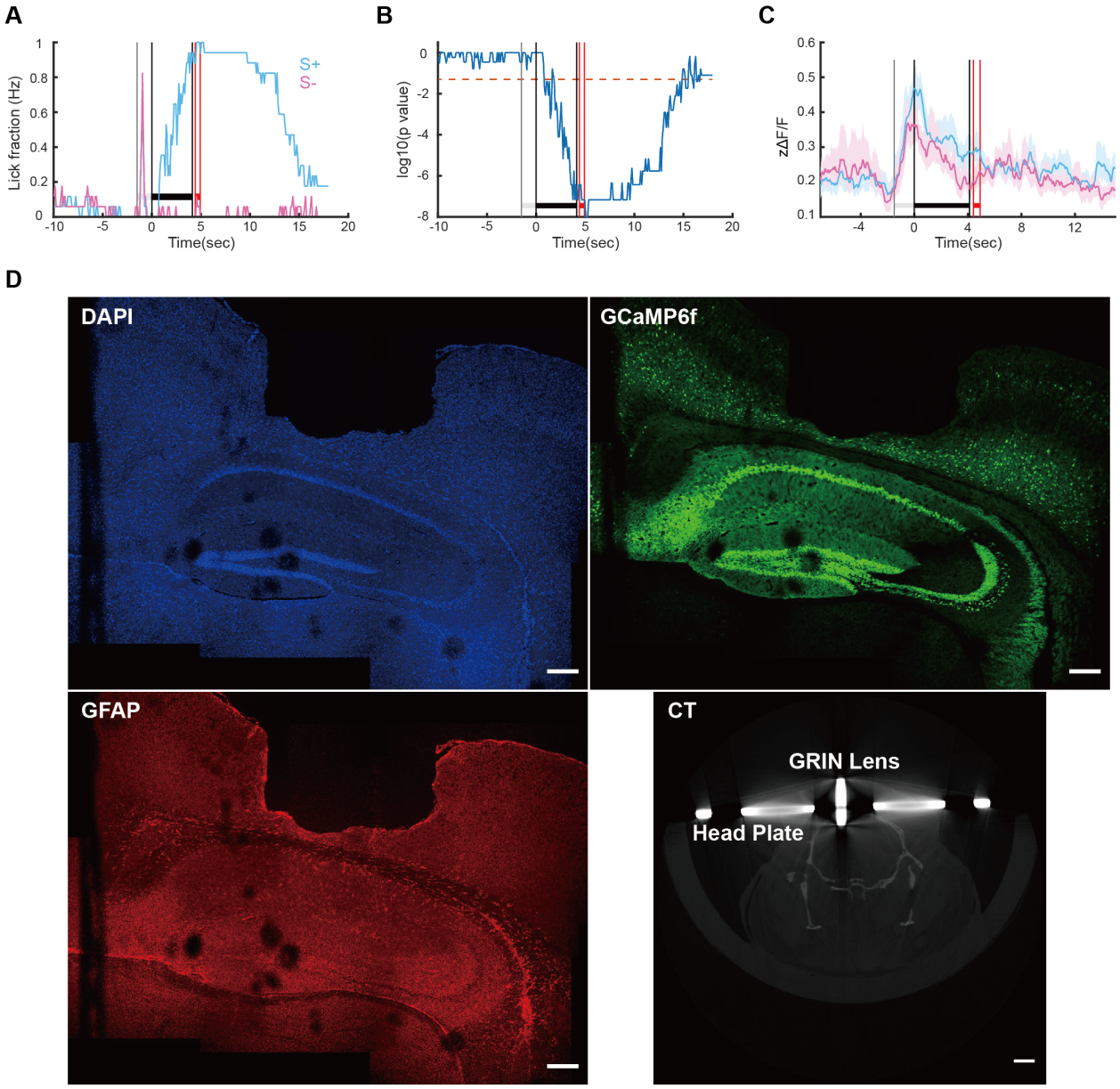

Figure S1. Supplementary data for Figure 1.

(A) Mean of lick fraction time course for S+ and S- trials for the session for the data shown in Figure 1.

(B) p value for a ranksum test comparing S+ vs. S- per trial lick time courses for the session for the data shown in Figure 1. The horizontal red line is p=0.05.

(C) Mean of per trial zΔF/F time course for S+ and S- trials for the session for the data shown in Figure 1.

(D) Immunofluorescence and CT scan showing the location of the GRIN lens in one mouse.

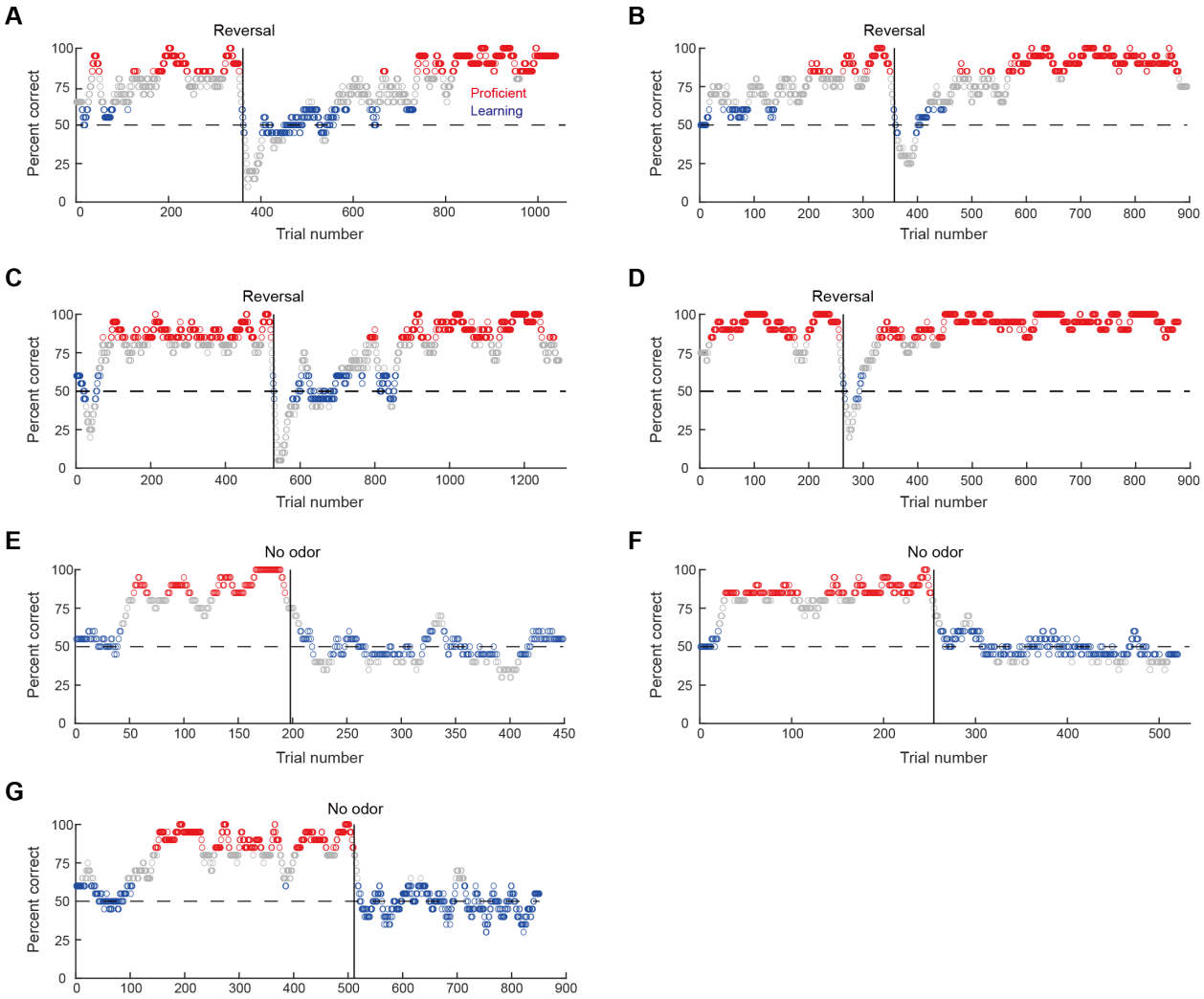

Figure S2. Behavioral performance of mice in the go-no go task.

(A to D) show the percent correct behavior calculated in a moving window of 20 trials for the entire training period for the four mice used in this study. Percent correct behavior is calculated as 100*(Hit trials+CR trials)/20. The trials with performance between 45 and 65 % correct (shown in blue) were classified as learning stage trials while the trials with performance at or above 80 % correct were classified as proficient (red). The task was started with heptanal (HEP) as S+ and mineral oil (MO) as S- (forward sessions). The

1496 vertical black line shows the point where these stimuli were reversed (MO became S+
1497 and HEP became S-, reversed sessions).
1498
1499 (E, F and G) show for three mice that the behavioral performance drops to 50% when the
1500 odorants are not delivered, but the odorant delivery valves still produce a click sound at
1501 the start of the trial (vertical line, no odor).
1502
1503

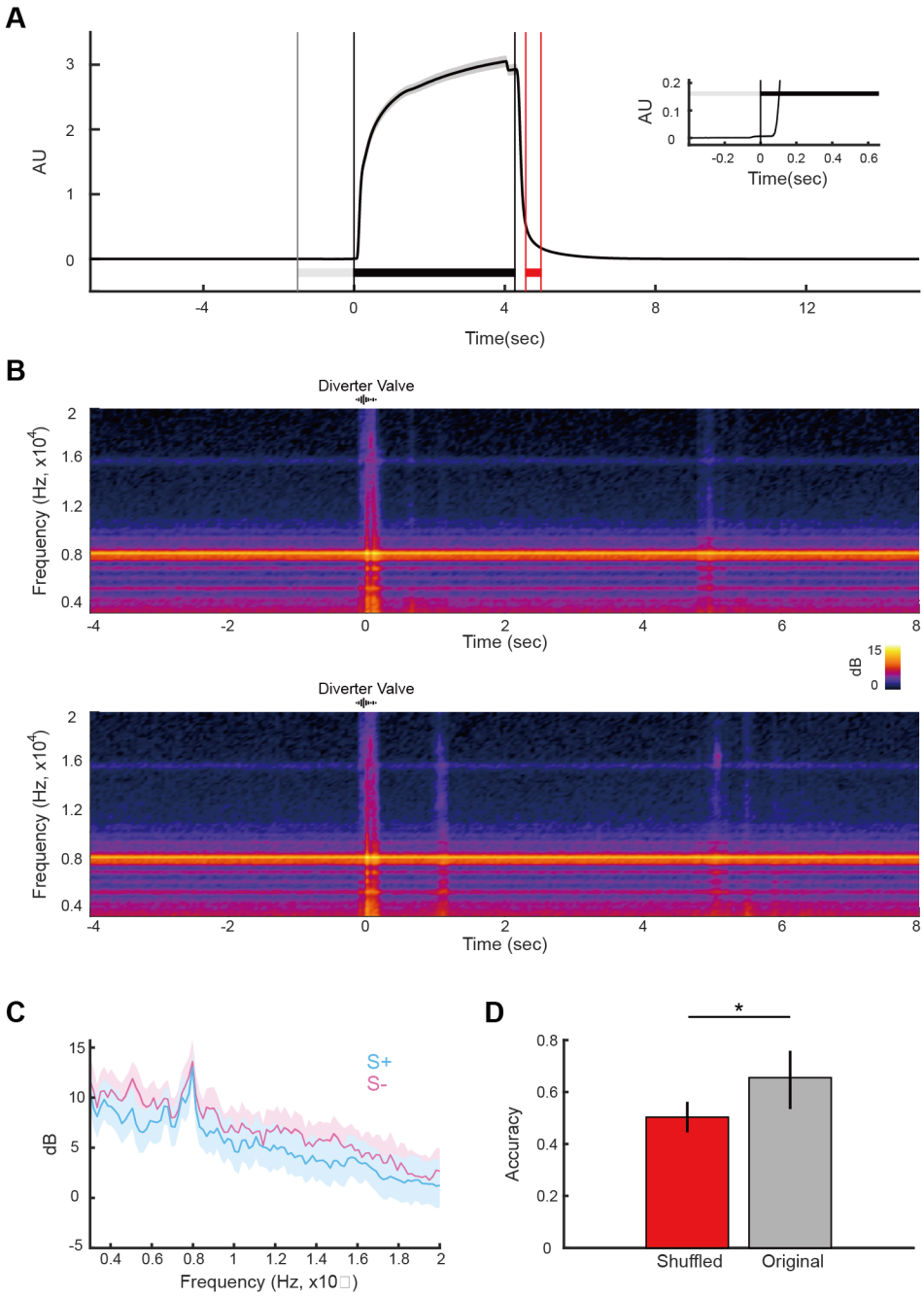

Figure S3. Time course for odorant onset and auditory cues.

(A) Increase in odorant concentration measured with a photoionization detector (PID). The inset shows that the onset of the increase in odorant concentration takes place ~100

msec after the diverter valve is turned off to deliver the odorant to the nose cone (time zero).

(B) Spectrogram time course for the mean sound power (in dB) for the clicks produced by the olfactometer for S+ and S- trials measured at the location where the mouse's head is in the 2P imaging enclosure. Time is referenced to the time point where the diverter and odor valves are turned on simultaneously (the start of the trial). Sound recording was performed in 30 S+ and 28 S- trials. The average power before diverter valve activation was subtracted from the power at each time point.

(C) Spectrogram for the mean sound power (in dB) measured at the time bin when the click occurred for the clicks produced by the olfactometer for S+ and S- trials measured at the location where the mouse's head is in the 2P imaging enclosure.

(E) Accuracy for decoding of trial type (S+ or S-) from sound power measured at the click. Decoding of trial type from sound power for clicks recorded in 30 S+ and 28 S- trials was performed using GLM with a leave one out procedure. As a control the labels (S+ or S-) were shuffled. A ranksum test yields a p value of 0.01 for the difference in per trial label prediction between shuffled and original (no shuffling) (n=58 trials).

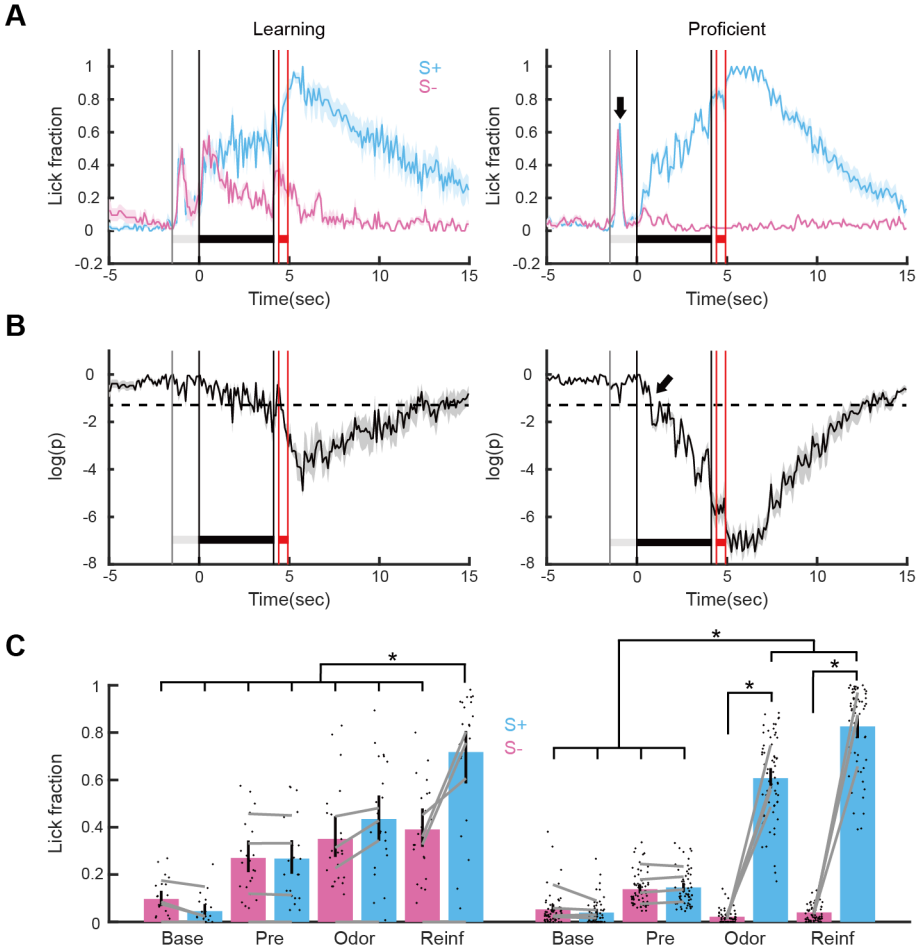

Figure S4. Lick responses for learning and proficient stages in the go-go task.

(A) Time course for lick fraction mean ± 95% CI for S+ and S- trials for all learning and proficient sessions (4 mice). Left: learning stage, right: proficient stage. Arrow points to the increase in lick fraction that takes place at the start of the trial.

(B) p value (mean ± 95% CI) calculated by a per time point ranksum test of the difference in lick fraction between S+ and S- trials (evaluated per session). The p value was calculated for all learning and proficient sessions (4 mice). The horizontal dashed line is

1543 p=0.05. The arrow points to the time when the p value decreases monotonically below
1544 0.05 for proficient mice.
1545 (C) Bar graph showing the mean value of lick fraction calculated in the following time
1546 windows: Base: -4.5 to -3.5 sec, Pre: -1 to 0 sec, Odor: 3.1 to 4.1 sec, Reinf: 4.5 to 5.5
1547 sec. Dots are lick fraction values per session and grey lines are lick fraction values per
1548 mouse.
1549
1550 *p<0.05 for a pFDR-corrected t-test or ranksum tests, GLM statistics are in Table S1.
1551

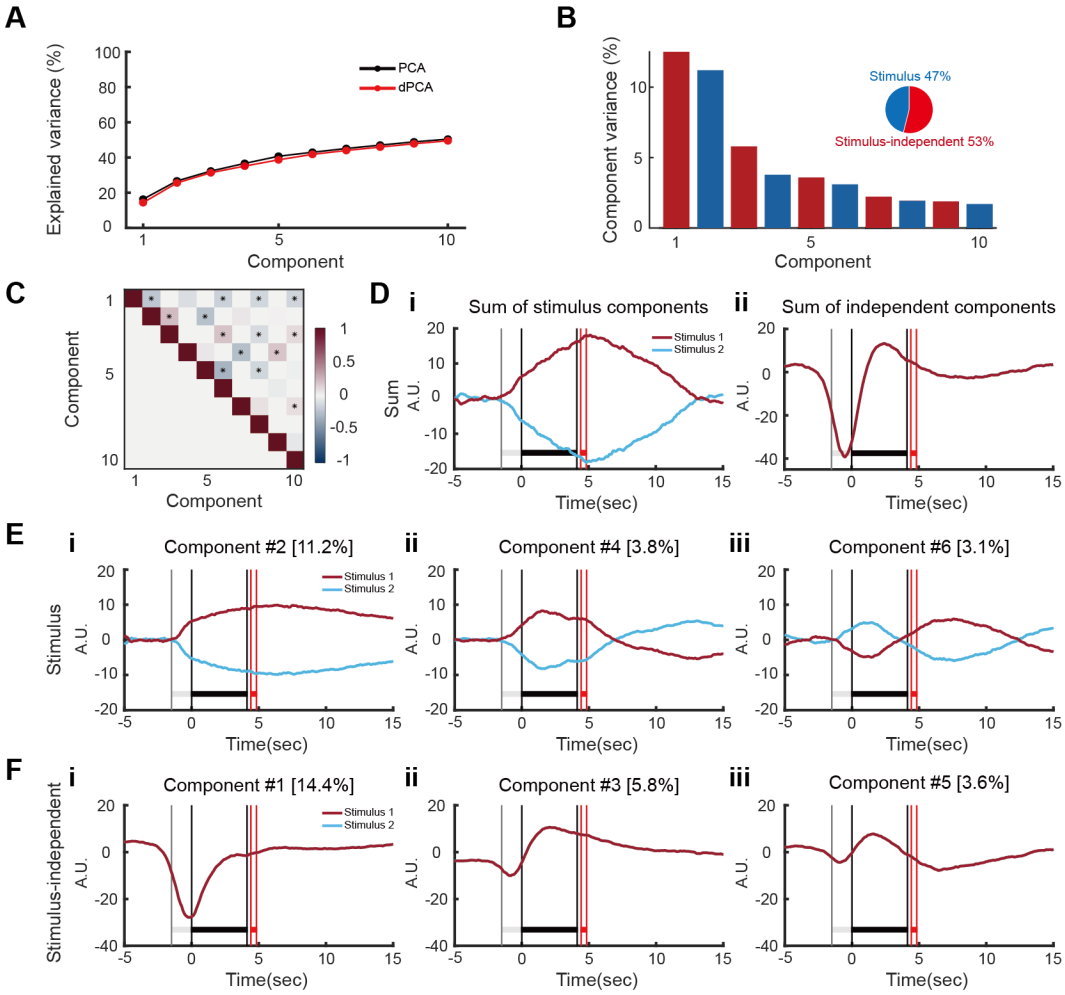

Figure S5. Example of demixed PCA for one mouse.

(A) Cumulative variance explained by PCA (black) and dPCA (red). Demixed PCA explains almost the same amount of variance as the standard PCA.

(B) Variance of the individual demixed principal components. Each bar shows the proportion of total variance, and is composed out of two stacked bars of different color: blue for

stimulus variance and red for stimulus independent variance. Pie chart shows how the total signal variance is split among parameters.

(C) Upper-right triangle shows dot products between all pairs of the first 15 demixed principal axes. Stars mark the pairs that are significantly and robustly non-orthogonal (see Materials and methods). Bottom-left triangle shows correlations between all pairs of the first 15 demixed principal components.

(D) Time course for the sum of all stimulus (i) or independent (ii) dPCA components

(E) Time course for the three top stimulus dPCA components

(F) Time course for the three top independent dPCA components

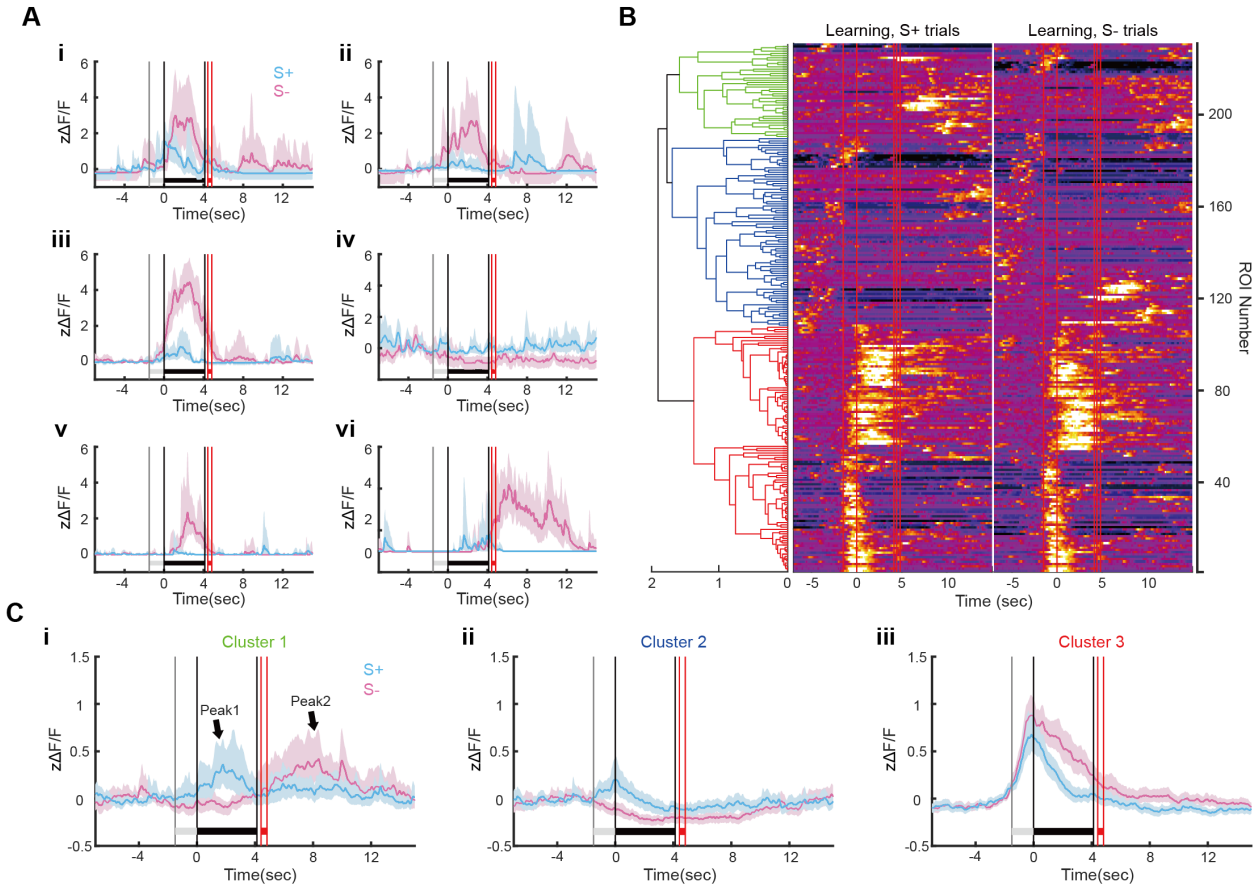

Figure S6. Stimulus-divergent zΔF/F responses for the learning stage and examples of zΔF/F responses that diverge between S+ and S- at different discrete time points after the start of the trial.

(A) Examples of zΔF/F time courses for single ROIs that differ in onset time for divergence between S+ and S- trials

(B) zΔF/F time courses for single ROIs that were divergent between S+ and S- trials in the learning sessions (18 sessions, 4 mice). Time courses were sorted by estimating an agglomerative hierarchical cluster tree shown on the left that was calculated using the cross correlation coefficients between all divergent zΔF/F time courses (not shown). The

red vertical lines show (in order): trial start, odorant on, odorant off, reinforcement on and reinforcement off.

(C) Mean zΔF/F time courses for the three clusters in the hierarchical tree shown in B.

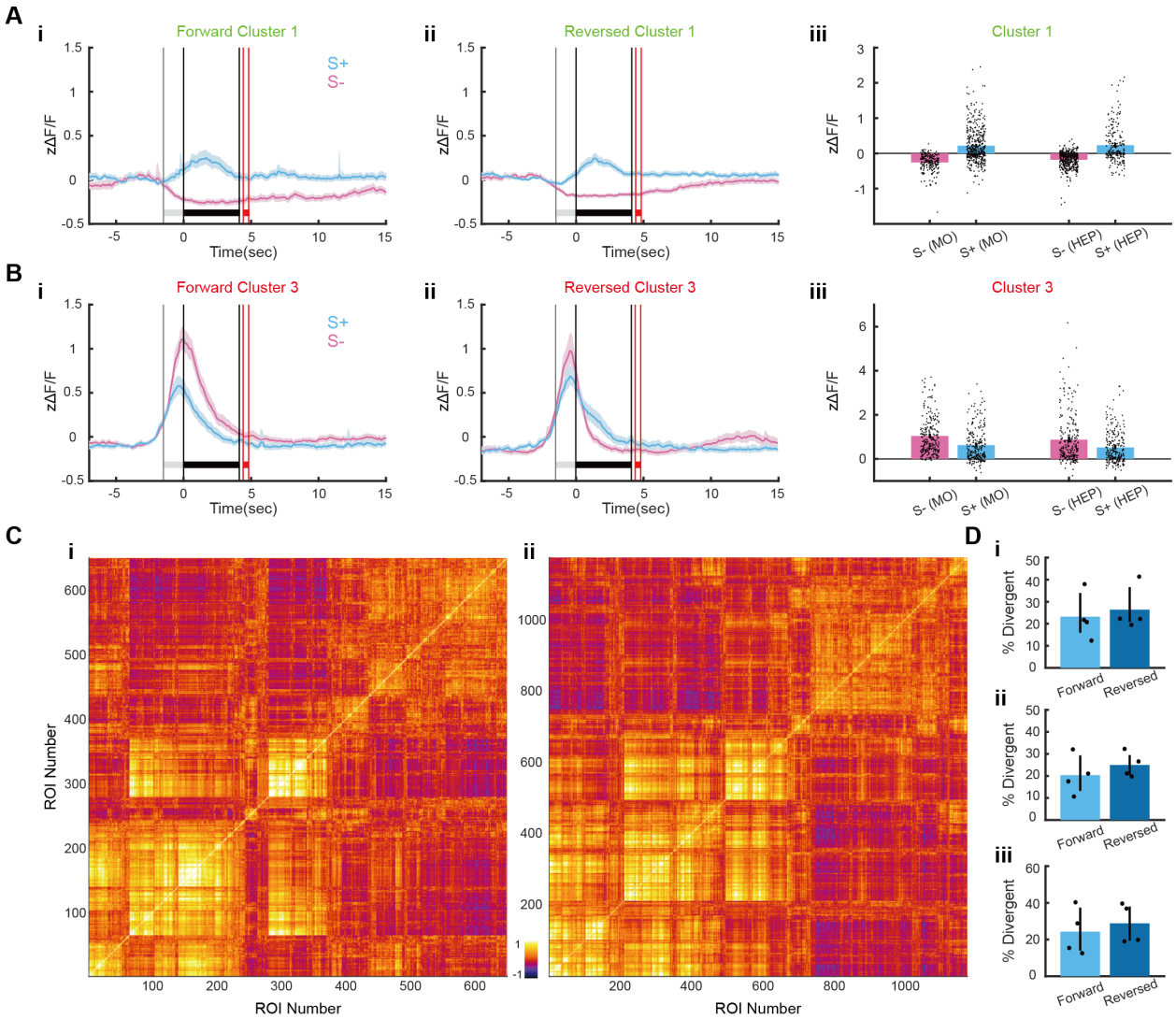

Figure S7. Supplemental data for Figures 5A and B characterizing changes in stimulus divergent zΔF/F responses after reversal of odorant valence.

(A and B) Mean zΔF/F time courses (i,ii) and peak zΔF/F (iii) for clusters 1 and 3 of the hierarchical cluster trees shown in Figures 5 A and B. Mean zΔF/F time courses for cluster 2 is Figure 5C. Table S6 shows the GLM statistical analysis for iii.

1606 (C) Cross correlation coefficients computed between all per trial zΔF/F time courses
1607 shown in Figures 5A and B. The coefficients were sorted by the agglomerative
1608 hierarchical cluster tree shown in those figures.
1609
1610 (D) i. Percent divergent ROIs per mouse for the data in Figures 5A and B. ii and iii. Percent
1611 responsive ROIs per mouse for S+ and S- trials. The percent divergent (i) and percent
1612 responsive (ii and ii) differences between learning and proficient stages were not
1613 statistically significant (two tailed t test $p>0.05$, $n=3$ for learning and 4 for proficient, 5 d.f.).
1614
1615

1616

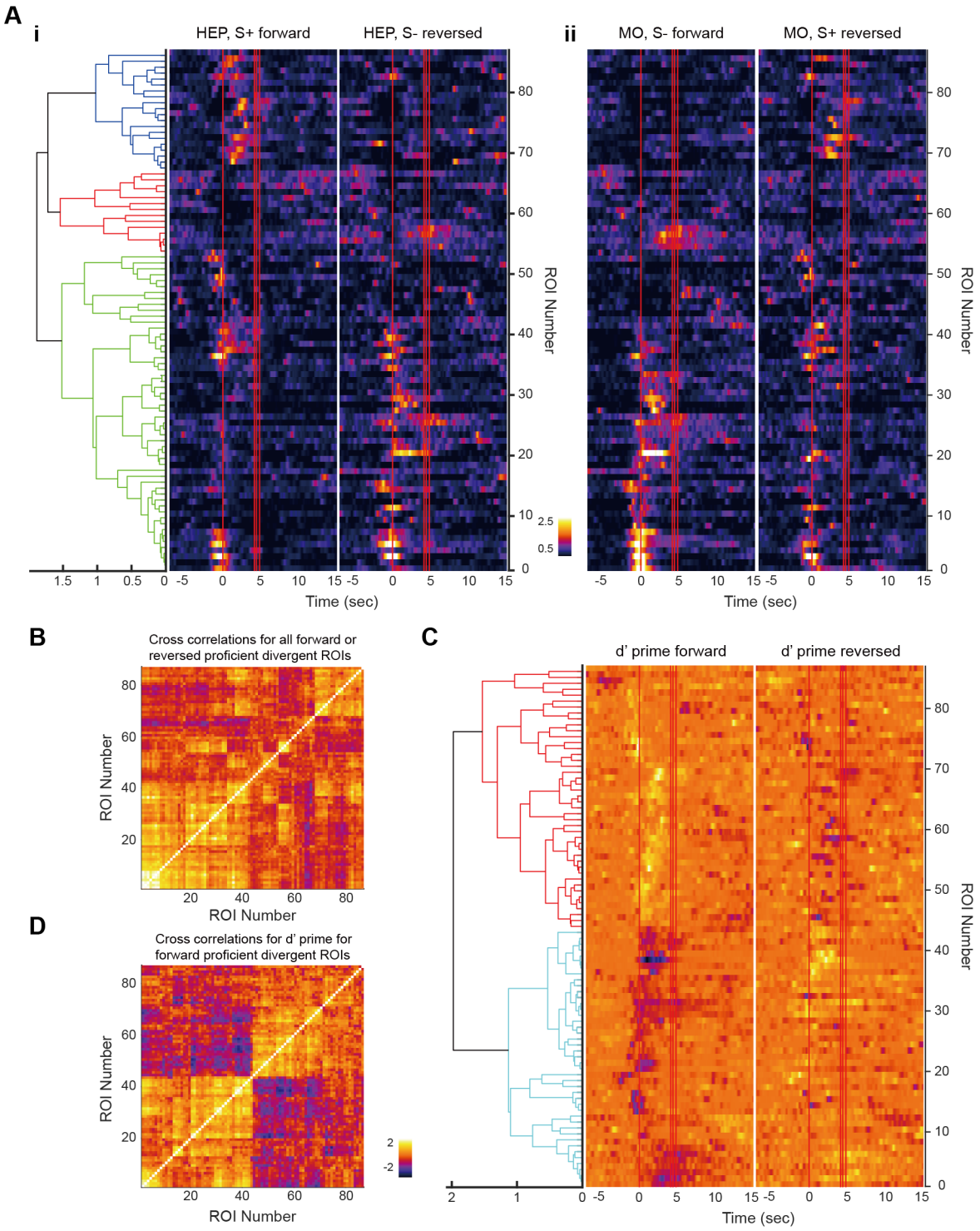
A
i
HEP, S+ forward
HEP, S- reversed
ii
MO, S- forward
MO, S+ reversed
ROI Number
Time (sec)
B
Cross correlations for all forward or reversed proficient divergent ROIs
ROI Number
D
Cross correlations for d' prime for forward proficient divergent ROIs
ROI Number
C
d' prime forward
d' prime reversed
ROI Number
Time (sec)

1617

Figure S8. Supplemental figure for Figure 5D characterizing zΔF/F for reversal calculated for one mouse with matched ROIs between forward and reversed sessions.

(A) zΔF/F time courses for single ROIs that were divergent between S+ and S- trials. (i) shows zΔF/F time courses for HEP in the forward and reversed proficient sessions (1 session) and (ii) shows zΔF/F time courses for MO in the forward and reversed proficient sessions (2 sessions). Time courses were sorted by estimating an agglomerative hierarchical cluster tree shown on the left that was calculated using the cross correlation coefficients between all divergent zΔF/F time courses (panel B). The red vertical lines show (in order): trial start, odorant on, odorant off, reinforcement on and reinforcement off.

(B) Cross correlation coefficients computed between all per trial zΔF/F time courses shown in Figure S8A. The coefficients were sorted by the agglomerative hierarchical cluster tree shown in that figure.

(C) zΔF/F d' time courses for single ROIs that were divergent between S+ and S- trials. (i) forward (1 session) and (ii) reversed (2 sessions) (d' was calculated for HEP vs. MO, see methods). Time courses were sorted by estimating an agglomerative hierarchical cluster tree shown on the left that was calculated using the cross correlation coefficients between all d' zΔF/F time courses (panel D). The red vertical lines show (in order): trial start, odorant on, odorant off, reinforcement on and reinforcement off.

1641

1642 (D) Cross correlation coefficients computed between all d' zΔF/F time courses shown in

1643 Figure S8C. The coefficients were sorted by the agglomerative hierarchical cluster tree

1644 shown in that figure.

1645

1646

1647

1648

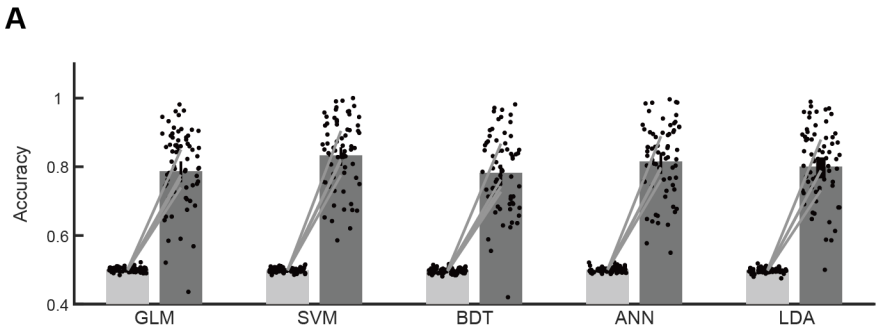

Figure S9. Stimulus decoding accuracy obtained by training in the wide odorant window with different decoding algorithms.

The bar graph shows the mean stimulus decoding accuracy obtained in the 3.1 to 4.1 sec window for different decoding algorithms trained with data in the 0.5 to 5.5 sec window for all proficient sessions (66 sessions, 4 mice, related to Figure 6). The different algorithms are: GLM: generalized linear model, SVM: support vector machine, BDT: binary decision tree, ANN: artificial neural network and LDA: linear discriminant analysis. A GLM analysis yields a statistically significant difference between GLM vs. SVM and GLM vs. ANN (n=684, 671 d.f., F-statistic 203, p-value <0.001, Table S11).

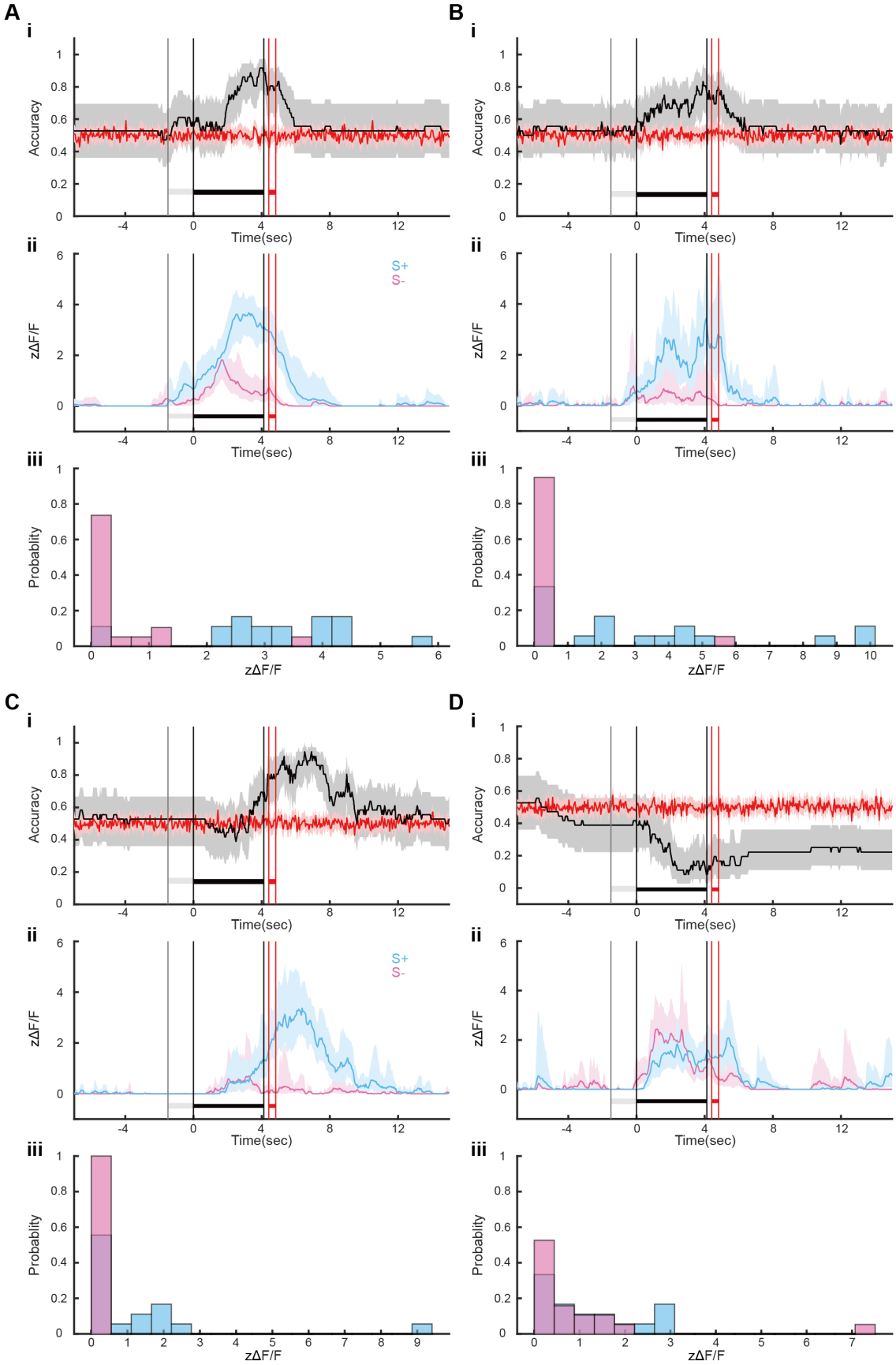

1662

Figure S10. Examples of single ROI stimulus decoding.

(A to D) show four examples of single ROI stimulus decoding. i. Decoding accuracy (black) vs. shuffled (red). ii. zΔF/F time courses for S+ (cyan) and S- (magenta). iii. Histogram of mean zΔF/F computed between 2 and 4.1 sec. This session had 62 ROIs with 18 S+ trials and 19 S- trials.

1669

1670

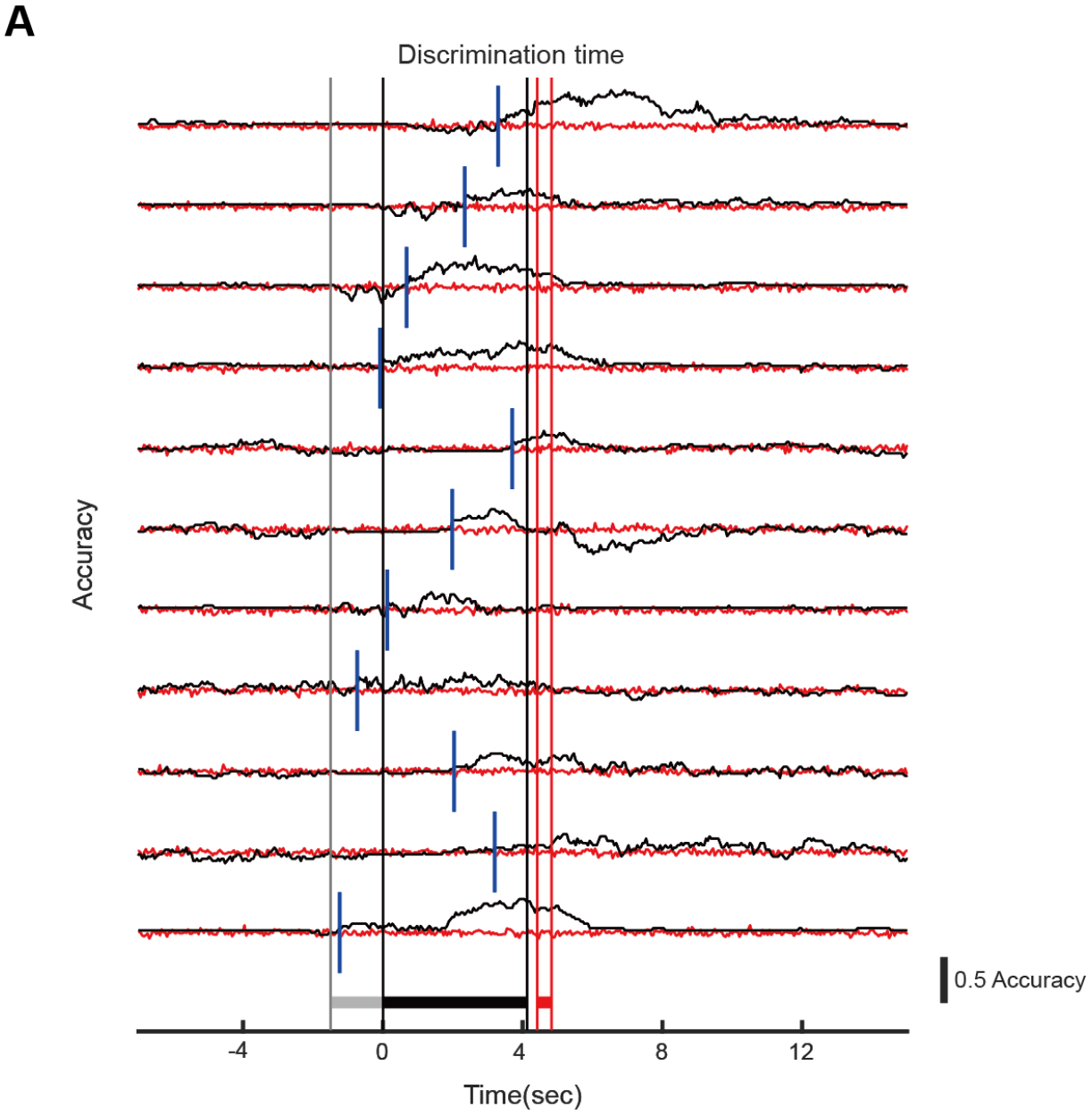

1671

1672 **Figure S11. Examples of stimulus decoding accuracy time courses for one session.**

1673 The figure shows stimulus decoding accuracy time courses for all ROIs that yielded

1674 accuracies > 0.65 for the proficient session of the examples shown in Figure S10.

1675

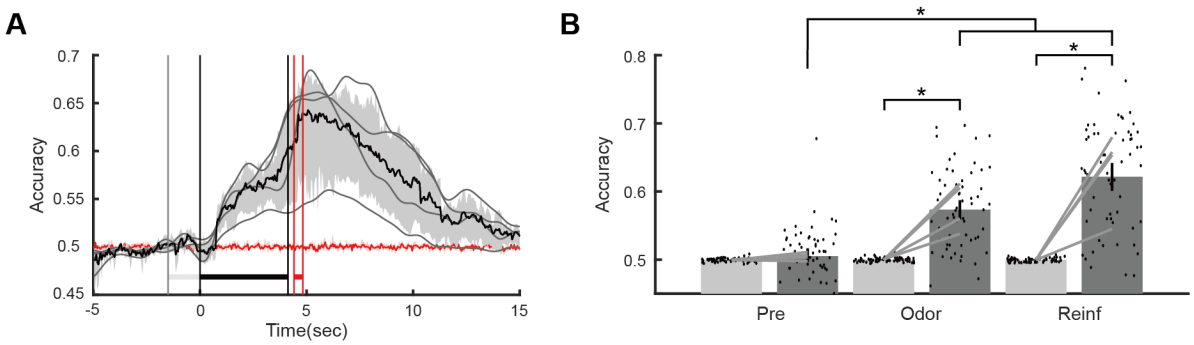

Figure S12. Lick decoding accuracy.

A. Time course per trial for the accuracy for ANN decoding of lick fraction from per trial z∆F/F responses for all trials and all ROIs per session for all proficient sessions (4 mice, 66 proficient sessions). The bounded black line represents the mean accuracy bounded by the 95% CI. The grey lines are per mouse accuracies. The red line is the stimulus decoding accuracy calculated after shuffling the stimulus labels (S+ vs S-).

B. Bar graph showing the mean accuracy for different accuracy periods (Pre -1 to 0, Odor 3.1 to 4.1 and Reinf 4.5 to 5.5). Light gray bars are the shuffled stimulus accuracies. Points are per session accuracies and bars are 95% CIs.

*p<0.05 for a pFDR-corrected t-test or ranksum tests, GLM statistics are in Table S10.

1690 **Video 1. Movie of fluorescence changes for CA1 pyramidal cells**

1691

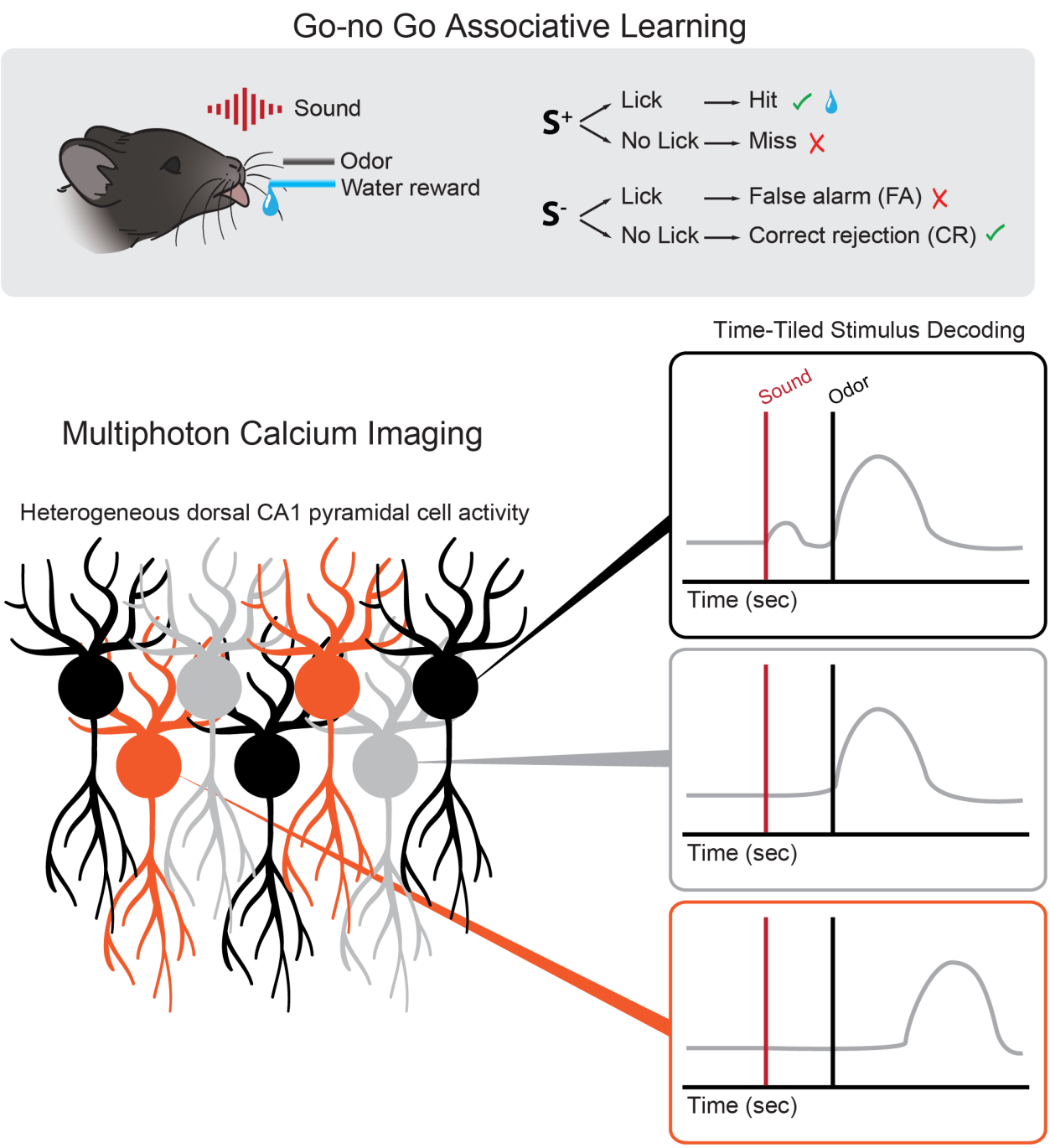

In Brief

Ma et al. show that the times for stimulus divergence of pyramidal cell neural activity in dorsal CA1 are time tiled during the mouse's response in a go-no go associative

learning odorant discrimination task. This sequential neural dynamics of decoding of odorant discrimination in dorsal CA1 would provide a cognitive time map for decision making in associative learning.

Highlights

- Spiking of pyramidal cells encodes for stimulus identity and lick behavior in dorsal CA1 for a mouse engaged in a go-no go odorant associative learning task
- The time of onset of stimulus divergence in neural activity of individual pyramidal cells in dorsal CA1 is time-tiled
- Learning increases the accuracy of decoding stimulus identity in this task
- The majority of pyramidal cells encode for odorant valence as opposed to odorant identity